On seismic gradiometric wave equation inversion for density

Marthe Faber [ID] and Andrew Curtis

University of Edinburgh, School of Geosciences, Edinburgh EH9 3FE, UK. E-mail: M.Faber@sms.ed.ac.uk

SUMMARY

Material density remains poorly constrained in seismic imaging problems, yet knowledge of density would provide important insight into physical material properties for the interpretation of subsurface structures. We test the sensitivity to subsurface density contrasts of spatial and temporal gradients of seismic ambient noise wavefields, using wave equation inversion (WEI), a form of seismic gradiometry. Synthetic results for 3-D acoustic media suggest that it is possible to estimate relative density structure with WEI by using a full acoustic formulation for wave propagation and gradiometry. We show that imposing a constant density assumption on the medium can be detrimental to subsurface seismic velocity images. By contrast, the full acoustic formulation allows us to estimate density as an additional material parameter, as well as to improve phase velocity estimates. In 3-D elastic media, severe approximations in the governing wave physics are necessary in order to invert for density using only an array of receivers on the Earth's free surface. It is then not straightforward to isolate the comparatively weak density signal from the influence of phase velocity using gradiometric WEI. However, by using receivers both at the surface and in the shallow subsurface we show that it is possible to estimate density using fully elastic volumetric WEI.

Key words: Inverse theory; Crustal imaging; Seismic noise; Rock physics.

1 INTRODUCTION

Dynamic processes in the Earth's shallow subsurface (top few 100 m) in which rocks, soil, atmospheric gases and meteoric water interact, are seldom well characterized and understood (Parsekian *et al.* 2015; Riebe *et al.* 2017). It is of interest for environmental and resource applications to better characterize these chemical and mechanical processes using information about heterogeneity in properties of the near-surface, so-called critical zone (Anderson *et al.* 2007). In critical zone studies, bulk density is an important physical property as an indicator for soil quality and compaction (Suuster *et al.* 2011). Lateral density variations can reveal information about changes in porosity, fracture distribution and soil weathering (Flinchum *et al.* 2022). Density is used to inform studies of root growth (Brimhall *et al.* 1992; Dexter 2004), water movement and retention (Huang *et al.* 2011; Flinchum *et al.* 2018), as well as carbon and nutrient content in soil layers (Nanko *et al.* 2014). It is therefore of significant interest to be able to estimate near-surface density.

Direct density measurements can be obtained via auger samples or Geoprobe coring (Holbrook *et al.* 2014). However, obtaining *in situ* measurements of bulk density at any significant depth is time-intensive and expensive, so it may be preferable to estimate density indirectly. So-called pedotransfer functions are used to predict bulk density based on regression models from soil measurement archives for the very shallow subsurface (<1 m; Suuster *et al.* 2011). Unfortunately, due to the sparsity of borehole samples from deep soil layers, few studies are able to estimate bulk density for deeper targets (Qiao *et al.* 2019). Well logs can be used to gain insight on bulk density and to infer porosity of the logged near-surface interval (Fanchi 2010; Holbrook *et al.* 2019), but remain invasive, localized and again expensive sources of information.

Geophysical methods complement direct observations. They allow larger and deeper subsurface volumes to be investigated, and temporal changes in properties to be monitored (Parsekian *et al.* 2015). Microgravity surveys are directly sensitive to density anomalies and are commonly used for environmental studies of the subsurface, for example to localize subsurface voids (Tuckwell *et al.* 2008) or for groundwater monitoring (Piccolroaz *et al.* 2015). However, this data type is strongly impacted by microseismic noise which might overshadow small signals related to mass distributions in the near surface (Boddice *et al.* 2022). Signals from density variations in the near surface soil (top 5 m) for example have been shown to be too weak to be detected by current gravity instrumentation, leading to lateral variations being obscured by the influence of deeper anomalies (Boddice *et al.* 2019). Furthermore, inversion procedures

for subsurface density on the basis of gravity data alone are inherently ill-posed (Blom *et al.* 2017). To reduce the non-uniqueness in such solutions, gravity measurements must be used in conjunction with other data types such as geological prior knowledge, well-log densities or seismic data, in order to produce realistic density maps (Nabighian *et al.* 2005).

Seismic imaging provides another non-invasive alternative to investigate the critical zone. Active methods such as seismic refraction tomography (Befus *et al.* 2011; Nielson *et al.* 2021; Flinchum *et al.* 2022) and multichannel surface wave analysis (Handoyo *et al.* 2022; Trichandi *et al.* 2022) are popular methods for imaging the near-surface. Seismic monitoring of dynamic processes may be achieved using omnipresent ambient seismic noise, a natural source of illumination in the Earth (Curtis *et al.* 2006; Obermann *et al.* 2015; Nakata *et al.* 2019), and dense arrays of seismometers may be used to provide a repeatable data source with high spatial resolution. Ambient noise seismology has thus allowed velocity changes over time to be monitored in the critical zone (James *et al.* 2019; Oakley *et al.* 2021).

Seismic methods usually focus on the retrieval of seismic velocities only, and are unable to isolate the signal corresponding to subsurface density unambiguously. Density values are often inferred via empirical relationships from the speed of *P* body-waves (e.g. Gardner *et al.* 1974) or less commonly from *S*-wave speeds (e.g. Miller & Stewart 1991), and estimating density as a seismic observable still remains a challenge. Body wave traveltime tomography exhibits an inherent insensitivity to density changes: body wave scattering caused by a density contrast characteristically propagates backwards rather than forwards, and so to first order does not interact with travel time measurements of forward propagating incident waves (Fichtner 2010). Surface waves, however, can be represented as an infinite sum of reflections and conversions between the free surface and subsurface interfaces, where the reflection coefficients depend on the density in the vicinity of the surface; this in turn affects the phase velocities of dispersive surface waves. Their frequency dependent arrival times are therefore sensitive to density variations in the subsurface, but the sensitivity is oscillatory with depth and can cancel destructively (Takeuchi & Saito 1972).

In the context of global seismology, where density plays an important role in explaining mantle dynamics, several studies have been conducted to invert for density from surface wave data. Nolet *et al.* (1977) showed that Rayleigh wave dispersion data are sensitive to the density structure in elastic media, as are normal modes at longer periods (Tanimoto 1991). It is however usually considered too challenging to estimate density in most elastic media using surface wave dispersion alone because the sensitivity is relatively weak compared to sensitivity to seismic velocity structure (Muyzert & Snieder 2000). Due to the poor constraints on density, it has been common practice in surface wave tomography to prescribe a scaling relation between density and shear velocity anomalies (Karato & Karki 2001) and to invert for velocity only. From seismological research, however, we know that anticorrelation of density and seismic velocity are observed: Resovsky & Trampert (2003) show that the long period seismic data clearly favour density perturbations that are poorly or negatively correlated with velocity heterogeneity. The uniform scaling of velocity and density in tomography arises under the assumption that density variations are purely thermal; this is not accurate for density variations related to compositional heterogeneities or liquid/gas inclusions (Płonka *et al.* 2016). Therefore, independent knowledge of density is important in order to discriminate between compositional and thermal

heterogeneities (Trampert *et al.* 2004; Mosca *et al.* 2012). Additional observables such as horizontal to vertical ratios (H/V) of surface waves can provide further constraints on density (Lin *et al.* 2012) but still show strong trade-offs with elastic parameters and velocity.

Variations in density generally have a smaller effect on the full, recorded seismic waveforms than variations in seismic velocity (Blom *et al.* 2017), and are subject to strong trade-offs with velocity which depend on the scattering angle of the wave (Luo & Wu 2018). Nevertheless, Płonka *et al.* (2016) show that realistic crustal density variations have measurable effects on seismograms. Density effects are mainly visible as amplitude changes, but also cause the waveform shape to be altered especially in the scattered wave train (Yuan *et al.* 2015; Blom *et al.* 2017). Hence, seismic methods that investigate the full seismic waveform such as full waveform tomography (Płonka *et al.* 2016; Blom *et al.* 2017, 2020) which includes both phases and amplitudes of body, surface and scattered waves, show promise to glean further constraints on subsurface density. However, in elastic multiparameter full waveform inversion (FWI), the highest ambiguity is attached to density regardless of the model parametrization employed (Köhn *et al.* 2012), and it is difficult to reconstruct density from full waveform inversion even using the dense data sets available in industrial exploration geophysics (Virieux & Operto 2009). Choi *et al.* (2008) successfully estimated density from 2-D elastic Marmousi models, but only using a low and narrow frequency band around 0.125 Hz. Pan *et al.* (2018) observed that *S*-wave velocity perturbations strongly contaminate density structure which can result in highly uncertain density estimates. Jeong *et al.* (2012) reports improvement in density recovery by implementing a 2-stage algorithm that estimates Lamé parameters with fixed density in a first step, and then inverts for density based on first stage velocity information in a subsequent step. Subsurface density of the ocean floor can be reliably estimated from real hydrophone data on the basis of a joint visco-acoustic FWI (Prieux *et al.* 2013; Operto & Miniussi 2018) and can be used as a background model to inform and reduce free parameters in elastic FWI. However, the performance of linearized FWI algorithms depends significantly on the availability of a well informed starting model (Virieux & Operto 2009; Vantassel *et al.* 2022).

Density affects the seismic wavefield mainly through reflection or backscattering. Hence, the strongest sensitivity of seismic waves is to spatial density contrasts or gradients (Blom *et al.* 2020). Hooke's law relates stress to strain, and strain is created by spatial wavefield gradients. In turn, stress can be related to density using Newton's second law, to form a so-called wave equation. This sparked interest in constraining density contrasts by deploying methods that are directly sensitive to amplitude changes in the wavefield gradients. Dense seismic arrays lend themselves well to the calculation of wavefield gradients using finite-difference methods.

A class of imaging techniques now termed seismic gradiometry (Curtis & Robertsson 2002; Langston 2007a, b; De Ridder & Biondi 2015) calculate temporal and spatial gradients of incoming waves or wavefields using dense array measurements to estimate physical subsurface parameters. A review of the theoretical background and applications of wave gradiometry methods can be found in Liang *et al.* (2023). One such method called wave equation inversion (WEI, Curtis & Robertsson 2002) substitutes the calculated gradients directly into the governing equation for wave propagation and provides estimates of local material properties via standard linear inversion techniques. By deploying a 3-D seismic array geometry with receivers recording all three components (3-C) of the wavefield, gradients can be estimated both horizontally at the surface

and with respect to depth (Fig. 1a). WEI can then be performed on the full elastic wave equation to estimate effective *P*- and *S*-wave velocities at the free surface. In an isotropic, locally homogeneous Earth, full elastic WEI is valid for any incoming wavefield; it thus has the advantage of being directly applicable to ambient seismic wavefields, but exhibits a high sensitivity to receiver positioning and orientation (Muijs *et al.* 2002; Vossen *et al.* 2004). A second type of gradiometric approach assumes a particular form or ansatz for the arriving wavefield [e.g. a single plane or spherically spreading wave (Fig. 1b)], and estimates parameters that describe the geometrical spreading and horizontal slowness (Langston 2007c, b). The method was applied for example as a new data processing technique for regional array seismology (Liang & Langston 2009; Liu & Holt 2015) and used to image the lunar near-surface structure (Sollberger *et al.* 2016). The method performs well for noiseless single source data, but gradiometry results based on the plane-wave assumption are highly sensitive to uncorrelated noise and to interference from other arriving waves (Langston 2007a). In order to use such methods in cases of unclassified wave type arrivals or ambient seismic noise, where two or more waves of similar amplitude and frequency are interfering, a statistical routine to identify individual interference-free events needs to be applied in advance (e.g. Edme & Yuan 2016). Alternatively a 'fingerprinting' technique based on 6C receiver measurements, which contain both translational and rotational ground motion, allows wave types of arriving seismic phases to be classified and individual arrivals from interfering wavefields to be isolated using machine learning methods (Sollberger *et al.* 2023).

In the case of an ambient seismic noise field, it is commonly assumed that surface waves are the dominating type of wave propagation. To capture the character of 2-D surface wave propagation, it is sufficient to record the wavefield with a dense receiver array at the Earth's surface (Fig. 1c). This relaxes requirements on the field acquisition geometry compared to volumetric gradiometry for which a 3-D array is necessary (Fig. 1a), while still allowing a wavefield comprising a superposition of plane waves arriving from different angles to be considered, instead of only individual plane waves as in Fig. 1(b). De Ridder & Biondi (2015) first approximated surface wave WEI on the basis of the 2-D Helmholtz wave equation which describes the propagation of surface waves at frequency dependent phase velocities (Wielandt 1993; Aki & Richards 2002). The method showed that phase velocity maps from the vertical component of ambient noise data at 0.7 Hz were comparable to results obtained using interferometric cross-correlations, thus validating the method. The method has since been extended to provide information on both isotropic and anisotropic local medium properties (De Ridder & Curtis 2017), and to near-real time applications (Cao *et al.* 2020).

The latter applications of surface wave WEI are based on the assumption that Rayleigh waves are the dominant wave type and that the 2-D scalar Helmholtz wave equation describes the recorded wavefield adequately (De Ridder & Biondi 2015; Cao *et al.* 2020). This is a significant approximation for seismic waves because the Helmholtz equation fails to describe general elastic wavefield dynamics. Since ambient noise recordings contain all kinds of interfering elastic wave types (including a variety of surface wave types and modes), the accuracy of subsurface material property estimates may be compromised. Nevertheless, Shaiban *et al.* (2022) used a synthetic 2-D elastic ambient noise wavefield to show that the correct local dispersion curves for a layered, laterally heterogeneous model could be estimated from the relationship between spatial and temporal gradients in the Helmholtz equation.

Surface wave WEI has been shown to require only a few minutes of ambient seismic noise recordings and rapid data processing after acquisition to produce useful phase velocity maps for the near-surface (at frequencies between 18 and 24 Hz), and so shows promise for efficient field deployment and near-real time monitoring purposes for the shallow subsurface (Cao *et al.* 2020). By estimating phase velocity maps for narrow bandpass filtered wavefields over a broad frequency range (depending on the ambient noise spectrum), the latter authors showed that 3-D images of a layered subsurface can be produced via inversion of local surface-wave dispersion curves for *S*-wave velocity (V_s) structure. 2-D shear-velocity maps for several depth levels up to 50 m were obtained in a matter of seconds from the dispersion curve through depth inversion performed by mixture-density neural networks. However, the quality of the 3-D shear velocity models are not only dependent on the accuracy of the phase velocity data but also on the impact of density in the inversion process (Ivanov *et al.* 2016). Dispersion-curve inversion for V_s is often implemented using predefined values for compressional-wave velocity (V_p) and density because their sensitivities to the phase velocity are much smaller than that of the *S*-wave velocity (Foti *et al.* 2018; Pan *et al.* 2019; Wu *et al.* 2020). Such *a priori* information on V_p is commonly obtained from other measurements, and density is often assumed to be constant (e.g. Cao *et al.* 2020) or inferred from empirical relationships with compressional wave speed (Gardner *et al.* 1974). Unfortunately, vertical density variations have been shown to affect the inverted V_s results, and the use of an inaccurate density background model can lead to false structures and overestimations in the V_s result (Ivanov *et al.* 2016). Expanding surface wave WEI to estimate the density structure of the subsurface and to quantify the effect of density gradients on the phase velocity estimates could therefore improve V_s models and seismic interpretation based on gradiometric methods.

In this study we investigate whether it is possible to estimate subsurface density on the basis of gradiometric surface wave WEI using ambient seismic noise. Both the accuracy in wave amplitude and shape are important considerations in gradiometric methods, and density heterogeneities were found to have an influence on both (Płonka *et al.* 2016; Blom *et al.* 2017). Hence, we expect to have sensitivity to the effect of density contrasts if we use data that record variations in wavefield amplitudes and phases.

In the Helmholtz formulation, which has been used in previous surface wave WEI studies, the wave equation does not exhibit an explicit sensitivity to density. In elastic media, the scalar Helmholtz wave equation is valid for surface waves only in laterally homogeneous media. In a realistic scenario, the subsurface is heterogeneous with velocity and density varying both laterally and with depth. In heterogeneous media, the superposition of multipathing surface waves propagates with a velocity that depends not only on the structural properties of the underlying medium, but also on the distribution of amplitudes of the interfering wavefield (Friederich *et al.* 2000). This implies that the Helmholtz wave equation is not a valid description for surface wave propagation and is likely to influence the accuracy of phase velocity estimates made via 2-D scalar WEI. In practice, if the medium is only smoothly heterogeneous, the Helmholtz equation is usually considered to be approximately valid for each surface wave mode separately. Seismic surface waves are then commonly approximated by acoustic waves, by assuming that the wavefield is purely dilatational and is dominated by pressure wave propagation. The acoustic approximations neglects mode conversions and the directivity of scattering from a point heterogeneity (Friederich *et al.* 2000), simplifying the mathematical model of wave propagation considerably.
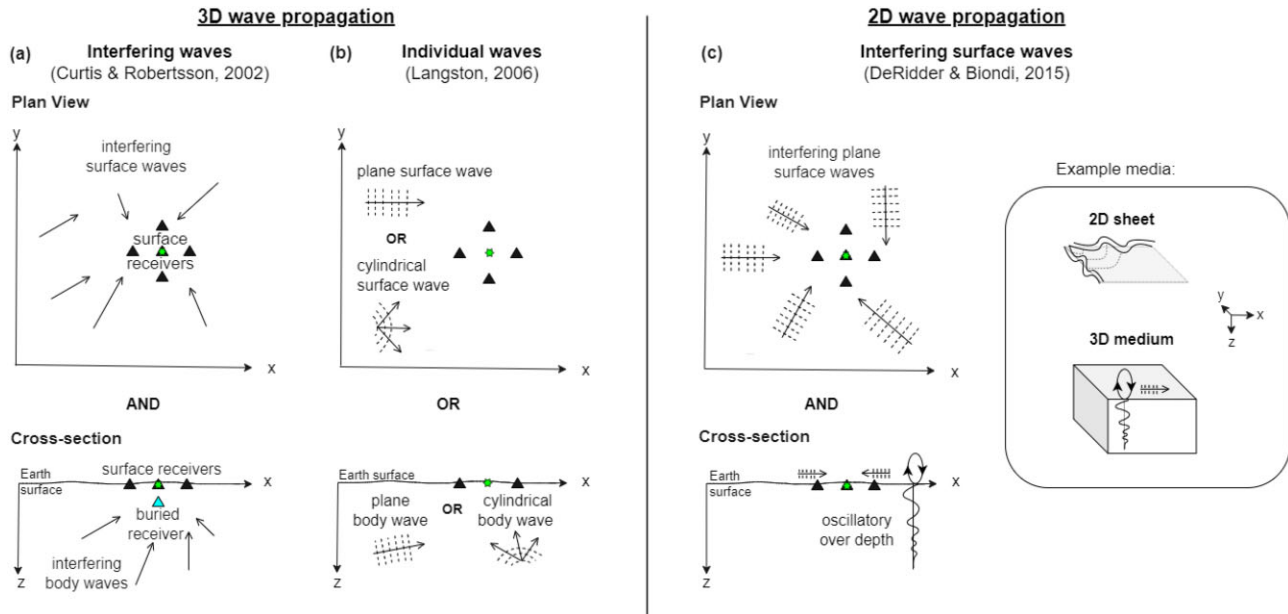
Figure 1. Schematic of acquisition geometries and physical assumptions made for different gradiometry types in plan view and cross-section view. Receivers are denoted by triangles and the configurations requiring the minimum number of receivers are shown to estimate gradients via classical finite difference around the central point (green star) with receivers recording translational motion. (a) The left-hand column shows principles of volumetric wavefield gradiometry as proposed by (Curtis & Robertsson 2002): with a 3-D receiver acquisition, second horizontal and vertical wavefield derivatives are approximated at a central point. To calculate derivatives in *x*-, *y*- and *z*-direction, 3-component (3C) receivers are necessary. Arrows denote interfering waves coming from all directions and angles; all wave types can be included in the wavefield, for example surface waves, body waves, scattered waves, etc. (b) Middle column shows gradiometry for non-interfering waves as proposed by (Langston 2007a). Individual plane or cylindrical waves can arrive from any direction at the receiver array. Receivers are used to estimate first horizontal derivatives of the wave field quantity; the central point does not require a recording. Receivers can be (1C) or (3C) depending on which wave type is analysed. Rotational sensors at the free surface allow for direct measurement of first derivatives (Schmelzbach *et al.* 2018; Sollberger *et al.* 2020). (c) Right-hand column shows principles of surface wave gradiometry as proposed by (De Ridder & Biondi 2015) where second order horizontal wavefield derivatives are approximated. This gradiometry type assumes a wavefield composed of interfering surface plane waves in a 3-D medium, or Lamb waves in a 2-D sheet (inset).

The scalar Helmholtz wave equation more accurately describes waves in acoustic media than in elastic media. In fact, in the acoustic case, the main simplification made in the derivation of the conventional scalar wave equation is that density is assumed to be constant across the local receiver array. To describe a more complex, physically more realistic medium, a variable density assumption can be introduced, which allows the acoustic medium to be described by a so-called full acoustic wave equation. The *full acoustic* wave equation was initially derived by Bergmann (1946) to define conditions under which density gradients in the atmosphere and large bodies of water should not be neglected in the governing wave equation formulation of sound pressure. The formulation of the full acoustic wave equation considered in that work assumes that gravity effects are negligible, and allows for density changes caused by either temperature gradients or changes in chemical composition of the material (Bergmann 1946).

In this paper, we first analyse wavefield sensitivities to subsurface density contrasts via WEI of the full-acoustic wave equation where density is treated as a variable. We expect the full acoustic formulation may allow us to analyse the role of density independently from wave speed. To test this hypothesis, we initially consider waves propagating through an acoustic medium so that the physics of that wave equation are consistent with the physics of the medium. We show that it is then possible to invert for density on the basis of full acoustic WEI and compare the effect of using the Helmholtz and full acoustic equation on phase velocity results in 3-D acoustic media. We then analyse whether the same procedure is applicable to elastic media despite the concomitant severe approximations to

the complex elastic wavefield physics. In elastic media, particle velocity is the natural wavefield observable rather than pressure, but we show that measuring pressure is necessary in order to relate the full acoustic wave equation approximation to the elastic case and to formulate an inverse algorithm that is explicitly sensitive to density. We then investigate whether volumetric gradiometry better lends itself to invert for density using the physically more representative full elastic wave equation at the free surface. By expressing the full elastic wave equation both in terms of pressure and displacement at the free surface we establish that a direct sensitivity to density exists and that density can be estimated.

2 WAVE THEORETICAL BACKGROUND

Density plays a different role in elastic and acoustic media. To illustrate, we compare the derivations of the respective governing wave equations from Newton's 2nd Law

$$\nabla \cdot \boldsymbol{\sigma} + \boldsymbol{f} = \rho \, \partial_t^2 \, \mathbf{u}, \qquad (1)$$

where $\boldsymbol{\sigma} = \sigma_{kl}$ is the stress tensor assuming k and l to range from 1 to 3 (for the *x*-, *y*- and *z*-directions), ρ is subsurface density, $\boldsymbol{f} = [f_x, f_y, f_z]^T$ is the distribution of applied body forces, $\mathbf{u} = [u_x, u_y, u_z]^T$ the observed wave field quantity of displacement or particle velocity and $\nabla = [\partial_x, \partial_y, \partial_z]^T$ in three dimensional media. The wave field quantity $\mathbf{u}$ is defined with respect to a reference state in which the medium is in equilibrium under gravity. It is well known that in isotropic elastic media and small displacements, Hooke's law allows stress to be expressed in terms of the strain tensor $\boldsymbol{\epsilon}$ (where

element $\epsilon_{xy} = \partial_x u_y + \partial_y u_x$ and similarly for other elements) and the Lamé parameters λ and μ which describe the medium's elasticity. This relationship can then be substituted into eq. (1), and similarly for acoustic media although the equations are then simpler because the shear modulus $\mu = 0$:

$$\nabla \cdot (\lambda \, tr(\epsilon) \, I + 2\mu\epsilon) \, + \, \boldsymbol{f} \, = \, \rho \, \partial_t^2 \, \mathbf{u} \quad \text{in elastic media} \quad (2a)$$

$$\nabla \cdot (\lambda \, tr(\epsilon) \, I) \, + \, \boldsymbol{f} \, = \, \rho \, \partial_t^2 \, \mathbf{u} \quad \quad \text{in acoustic media} \quad (2b)$$

where $tr()$ is the trace operator. By substituting expressions for elements of ϵ into eqs (2a) and (2b) we obtain the familiar 3-D elastic wave equation for isotropic, locally homogeneous media and a description of pressure wave propagation in terms of the wave field quantity $\mathbf{u}$, respectively:

$$- \frac{\mu}{\rho} [\nabla \times (\nabla \times \boldsymbol{u})] + \frac{(\lambda + 2\mu)}{\rho} [\nabla(\nabla \cdot \boldsymbol{u})] + \frac{\boldsymbol{f}}{\rho}$$
$$= \partial_t^2 \, \mathbf{u} \quad \quad \text{in elastic media} \quad (3a)$$

$$\frac{\lambda}{\rho} [\nabla(\nabla \cdot \boldsymbol{u})] + \frac{\boldsymbol{f}}{\rho} \, = \, \partial_t^2 \, \mathbf{u} \quad \text{in acoustic media.} \quad (3b)$$

In this paper, we focus on the case in which we would like to use ambient seismic noise, so we assume an absence of strong local sources in the area of wavefield recording and henceforth omit source term $\boldsymbol{f}$ (we discuss the introduction of suitable force terms in Section 7). In acoustic media, the first Lamé parameter λ is the acoustic bulk modulus K_a, whereas the bulk modulus in elastic media is $K_e = \lambda + \frac{2}{3}\mu$. In elastic media, density is expressed only in combination with the Lamé parameters within the terms equating to P-wave velocity $v_{P,e} = \sqrt{(\lambda + 2\mu)/\rho}$ and S-wave velocity $v_{S,e} = \sqrt{\mu/\rho}$ in eq. (3a), and similarly for acoustic media. This implies that while it may be possible to estimate the velocities from waveform data $\boldsymbol{u}$, it will not be possible to discriminate the Lamé parameters from the density since any velocity value can be fit by any reasonable density given a suitable choice of λ and μ.

In acoustic media, we often measure pressure P rather than wavefield displacement or particle velocity. The particle velocity field can then be estimated from this measured pressure field (Robertsson & Kragh 2002; Amundsen *et al.* 2005). Pressure is directly related to the divergence of the wavefield displacement $\mathbf{u}$ via $P = K_a \nabla \cdot \boldsymbol{u}$, where K_a is the bulk modulus in acoustic media. By applying a divergence operator to both sides of the acoustic wave eq. (3b) it is possible to express the sensitivity of measurements of pressure P to density ρ explicitly:

$$\nabla \cdot \left(\frac{K_a}{\rho} [\nabla(\nabla \cdot \boldsymbol{u})] \right) \, = \, \nabla \cdot \partial_t^2 \boldsymbol{u} \quad (4)$$

$$\Rightarrow \, v_{P,a}^2 \, \rho \, \nabla \cdot \left(\frac{1}{\rho} \nabla P \right) \, = \, \partial_t^2 P, \quad (5)$$

where in eq. (5) we have used the definition of P-wave velocity in acoustic media $v_{P,a} = \sqrt{K_a/\rho}$. Since density appears separately from P-wave velocity and has a different relationship to the measurable right-hand side of eq. (5), we expect a potentially distinguishable density signature in seismic waves travelling through heterogeneous media in which the spatial derivative of density on the left is non-zero.

Cance & Capdeville (2015) show how elastic and acoustic wave equations can be related in an isotropic, homogeneous domain for an explosive isotropic source emitting only P waves. In such a case, the curl of the wavefield is equal to zero ($\nabla \times \boldsymbol{u} = 0$) and any vector field such as the displacement $\boldsymbol{u}$ or the particle velocity field $\boldsymbol{v} = \partial_t \boldsymbol{u}$ can be derived from a potential Φ (Kaufman *et al.* 2000).

The potential Φ may be chosen as in Cance & Capdeville (2015) to be

$$\boldsymbol{u} \, = \, \frac{1}{\rho} \, \nabla \Phi, \quad (6)$$

where Φ is directly related to acoustic pressure via the relationship $\Phi = -2P_e$ and where the pressure wavefield P_e in elastic media is

$$P_e = -\frac{1}{2} K_a \nabla \cdot \boldsymbol{u}. \quad (7)$$

Substituting eq. (6) into eq. (3a) yields,

$$\frac{\lambda + 2\mu}{\rho} \nabla \left[\nabla \cdot \left(\frac{1}{\rho} \nabla \Phi \right) - \frac{1}{\lambda + 2\mu} \partial_t^2 \Phi \right] \, = \, 0 \quad (8)$$

$$\nabla \cdot \left(\frac{1}{\rho} \nabla \Phi \right) - \frac{1}{\lambda + 2\mu} \partial_t^2 \Phi \, = \, \text{const.} \quad (9)$$

Since eq. (8) holds everywhere and so the constant is independent of position of the recording, and because the wavefield is absent (has zero energy) at infinity (Kaufman *et al.* 2000), eq. (9) gives the potential equation in elastic media,

$$c_\omega^2 \, \rho \, \nabla \cdot \left(\frac{1}{\rho} \nabla \Phi \right) \, = \, \partial_t^2 \Phi, \quad (10)$$

where c_ω is the phase velocity at frequency ω. Eq. (10) describes 'acoustic' wave propagation in elastic media and is the elastic equivalent of eq. (5) for acoustic media.

The above equations show that different seismic observables interact differently with the subsurface: to isolate the effect of density from wave speed in elastic media on the basis of the full acoustic approximation or the elastic wave equation at the free surface, it is necessary to measure pressure instead of particle displacement or velocity (eqs 6–10) because pressure implicitly includes a power of K_a which changes the form of the respective equations. Classical seismometers only measure particle velocity, from which displacement can be calculated by time integrating the data, whereas elastic pressure is usually not observed on land. The expression for pressure is proportional to the divergence of the displacement (eq. 7) which can be determined from four geophone recordings at the Earth's free surface using gradiometry (Robertsson & Muyzert 1999; Shapiro *et al.* 2000; Robertsson & Curtis 2002). Given that stress is equal to zero across the free surface, the vertical derivative of the wavefield can be expressed in terms of horizontal derivatives [e.g. see eq. (14) further below]. This results in the wavefield divergence taking a modified form that can be written in terms of the Lamé parameters and the horizontal wavefield components only $\nabla \cdot \boldsymbol{u} = (2\mu/(\lambda + 2\mu)) \nabla_H \cdot \boldsymbol{u}_H$, where $\nabla_H = [\partial_x, \, \partial_y]^T$ and $\boldsymbol{u}_H = [u_x, u_y]^T$ (e.g. Maeda *et al.* 2016). However, calculating the divergence alone is not sufficient to isolate density in the wave equations because the bulk modulus is not accounted for as it is in the full pressure measurement (eq. 7).

Edme *et al.* (2018) suggest that it is possible to measure pressure directly at the free surface of an elastic medium with a land hydrophone. The land hydrophone is insensitive to the direction and angle of incoming waves which makes it predominantly sensitive to pressure fluctuations induced by ground-roll (more specifically, S-to P-conversions generated by upcoming S waves) due to destructive summation of events at near vertical incidence angle. At the free surface of the Earth, elastic pressure $P_{e,FS}$ can be written in terms of displacement in a 2-D plane and its horizontal derivatives as (Edme *et al.* 2018)

$$P_{e,FS} \, = \, K_{e,FS} \nabla_H \cdot \boldsymbol{u}_H \, \approx \, 0.37 \, K_a \nabla_H \cdot \boldsymbol{u}_H \quad (11)$$

where the elastic bulk modulus at the free surface is $K_{e,FS} = 2\rho\, v_S^2\, (1 - 4\, v_S^2/3\, v_P^2)$ and v_P and v_S are the local *P*- and *S*-wave velocities, respectively. The elastic pressure at the free surface can be related to acoustic pressure using $v_P = \sqrt{3}v_S$ for a Poisson solid. The measured pressure thus corresponds to the volume change caused by the dilatational part of surface wave propagation.

Acoustic pressure caused purely by *P*-wave propagation in a non-rotational medium has a similar expression to elastic pressure at the free surface of the Earth caused by the dilatational part of surface wave propagation. Surface waves can only be produced in a medium where rotation exists, and are generated by *P*- and *S*-wave interactions upon reflections and scattering at medium heterogeneities. Their propagation is mostly driven by *S* waves which correspond to the purely rotational part of the wavefield. Nevertheless, Rayleigh waves do exhibit dilatational wave propagation that produces a measurable pressure field at the free surface. The full acoustic approximation is only valid for elastic *P* waves in a homogeneous, isotropic medium, and is compromised in heterogeneous or anisotropic media due to *P*-to-*S* conversions. *P* waves and the *P* component of Rayleigh waves therefore presumably interact differently with the medium and might exhibit different sensitivities to different subsurface parameters such as subsurface density. Cance & Capdeville (2015) found that acoustic and elastic pressure are not the same for rough, heterogeneous media: a good agreement can only be achieved in homogeneous or weakly heterogeneous, smooth media. This suggests that in a realistic subsurface problem, inverting for the parameters on the basis of an acoustic approximation might be too approximate an approach to obtain sufficiently accurate information about elastic subsurface parameters by measuring pressure. We test this in what follows.

In elastic media it is not strictly necessary to consider the acoustic approximation in order to isolate density by substituting pressure. If we introduce the free surface conditions

$$\partial_z u_x = -\partial_x u_z \qquad (12)$$

$$\partial_z u_y = -\partial_y u_z \qquad (13)$$

$$\partial_z u_z = -\frac{v_{P,e}^2 - 2v_{S,e}^2}{v_{P,e}^2}\,(\partial_x u_x + \partial_y u_y) \qquad (14)$$

which express the fact that stress across the free surface must be zero, then equation (3a) can be written in a modified form that is valid at the free surface and in the absence of body forces (Curtis & Robertsson 2002):

$$\partial_z^2 u_x = \frac{\partial_t^2 u_x}{v_{S,e}^2} - \left(\nabla_H^2 u_x\right) - 2\left(1 - \frac{v_{S,e}^2}{v_{P,e}^2}\right)\partial_x(\nabla_H \cdot \boldsymbol{u}_H) \qquad (15)$$

$$\partial_z^2 u_y = \frac{\partial_t^2 u_y}{v_{S,e}^2} - \left(\nabla_H^2 u_y\right) - 2\left(1 - \frac{v_{S,e}^2}{v_{P,e}^2}\right)\partial_y(\nabla_H \cdot \boldsymbol{u}_H) \qquad (16)$$

$$\partial_z^2 u_z = \frac{\partial_t^2 u_z}{v_{P,e}^2} + \left(1 - 2\frac{v_{S,e}^2}{v_{P,e}^2}\right)\nabla_H^2 u_z. \qquad (17)$$

Even though a free-surface is usually referred to as the interface of a half-infinite elastic medium in contact with vacuum (Robertsson *et al.* 1995), free-surface conditions are a reasonable approximation on Earth given that the subsurface has elastic properties and the contact layer is air which has low density. In the case of granular medium (such as regolith) or in heavy atmospheres, the free-surface condition would need to be updated with more appropriate constraints.

By using a so-called Lax–Wendroff derivative centering technique (Lax & Wendroff 1964; Blanch & Robertsson 1997; Curtis & Robertsson 2002), the first order vertical derivative can be correctly

represented at the free surface by a finite difference approximation to horizontal spatial derivatives. Using a 3-D receiver array as proposed in Fig. 1(a) it then becomes possible to approximate all quantities necessary to estimate body wave velocities at the free surface. For example, a new expression can be derived for the vertical displacement component in eq. (17) by using the free-surface condition (14) and the Lax–Wendroff corrected finite difference depth derivative:

$$\partial_t^2 u_z = v_{P,e}^2\, A_z(t) - v_{S,e}^2\, B_z(t), \qquad (18)$$

where $A_z(t)$ and $B_z(t)$ are expressions containing finite difference approximations to derivatives of the wavefield

$$A_z(t) = \frac{2}{\Delta z}\left(\nabla_H \cdot \boldsymbol{u}_H + [\partial_z u_z]_{fd}\right) - \nabla_H^2 u_z \qquad (19)$$

$$B_z(t) = \frac{4}{\Delta z}\left(\nabla_H \cdot \boldsymbol{u}_H\right) - 2\left(\nabla_H^2 u_z\right) \qquad (20)$$

and where Δz is the distance between the surface and the buried receiver, and $[\partial_z u_z]_{fd}$ is the first order finite difference depth derivative. The derivation of these expressions is described in detail in Curtis & Robertsson (2002), and herein, we only consider constraints derived from the vertical displacement component as they were shown to better constrain body wave velocity estimates than those derived from horizontal components. Furthermore, inhomogeneous terms arising from variations in subsurface parameters do not play a role in the vertical component at the free surface, making the expressions valid for any type of elastic medium without approximations (Appendix E).

By using the relation $P = P_{e,FS}/0.37$ from eq. (11), acoustic pressure can be substituted into eqs (19) and (20):

$$A_z'(t) = \frac{2}{\Delta z}\left(\frac{1}{K_a}P + [\partial_z u_z]_{fd}\right) - \nabla_H^2 u_z \qquad (21)$$

$$B_z'(t) = \frac{4}{\Delta z}\frac{1}{K_a}P - 2\left(\nabla_H^2 u_z\right). \qquad (22)$$

Feeding the expressions for $A_z'(t)$ and $B_z'(t)$ into eq. (18) we obtain

$$\partial_t^2 u_z + v_{P,e}^2\left[-\frac{2}{\Delta z}[\partial_z u_z]_{fd} + \nabla_H^2 u_z\right] - 2v_{S,e}^2 \nabla_H^2 u_z$$
$$= \frac{1}{\rho}\left[\frac{1}{\Delta z}\left(2 - \frac{4v_{S,e}^2}{v_{P,e}^2}\right)P\right]. \qquad (23)$$

Displacement measurements are all on the left-hand side and pressure measurements on the right-hand side of eq. (23); in order to use this equation to constrain the velocities and density, both displacement and pressure must be measured simultaneously at the free surface. An explicit sensitivity becomes clear from eq. (23) with density connecting the left- and right-hand sides of the equation linearly.

3 GRADIOMETRIC METHODOLOGY

Herein, we focus on the potential of gradiometric methods based on 2-D surface arrays [similarly to De Ridder & Biondi (2015) in Fig. 1c] and 3-D volumetric arrays [similarly to Curtis & Robertsson (2002) in Fig. 1a] to estimate density in addition to the medium's wave speed. We start outlining the 2-D gradiometric methodology (Section 3.1) for density inversion in light of eqs (5) and (10). These equations are naturally suitable for acoustic wave propagation, but are subject to restrictive and potentially unrealistic assumptions in elastic media. We investigate whether a practical 2-D array setup, that limits the complexity of the wave equation that can be used for

WEI (vertical wavefield gradients can not be measured for example), yields sufficient information to estimate density in an acoustic medium where the physics fits the used eqs (5) and (10), and to extend the method to elastic media. We then test whether using a 3-D array configuration (Section 3.2) that includes an additional buried receiver, and which makes it possible to use a physically more appropriate equation for elastic wavefield data (i.e. eq. 23), improves the density estimates in elastic media. The following subsections are therefore ordered according to the gradiometric WEI approach used for density estimation—using free surface and then volumetric array recordings (Sections 3.1 and 3.2, respectively).

3.1 Free surface arrays

In previous wavefield gradiometry studies performed with data from 2-D receiver arrays on the Earth's surface, the role of density has been neglected. If density is assumed to be constant over space, eq. (10) reduces to the scalar Helmholtz wave equation, the 2-D version of which is usually used as a basis for WEI where ∇ is used as a 2-D operator ($\nabla = \nabla_H = [\partial_x, \partial_y]^T$) and $\boldsymbol{x} = [x, y]^T$:

$$c_\omega(\boldsymbol{x})^2 \nabla^2 \theta(\boldsymbol{x}, t) = \partial_t^2 \theta(\boldsymbol{x}, t). \tag{24}$$

Here, θ denotes any type of wavefield quantity (e.g. one component of the wavefield displacement or particle velocity field, or the pressure field) which varies as a function of horizontal position x and y and time t. This equation is a major approximation of how seismic waves actually propagate in the Earth's subsurface: all 3-D propagation of elastic body waves and of different types of surface waves, each associated with multicomponent particle motions, are approximated by a single wave type propagating in 2-D across the Earth's surface with a single independent component of particle motion. For example, in isotropic media Love waves are horizontally polarized and arrive most prominently on the transverse component, whereas the Rayleigh waves are polarized in a vertical plane and appear mainly on the vertical and radial components (Shearer 2019). In the case of ambient noise, we deal with complex wavefields arriving from multiple sources which makes it impossible to distinguish radial contributions from transverse contributions; Love and Rayleigh waves therefore interfere in the horizontal particle velocity field yet are treated as one wave type in the 2-D scalar wave equation. On land therefore, 1C geophone recordings are usually used as gradiometric measurements, because Rayleigh waves typically dominate the ambient seismic noise field and predominantly excite vertical displacements. A similar argument applies to Scholte waves which travel along the water-seabed interface. And since surface waves predominantly travel across the Earth's surface and have a dominant mode number, they are commonly approximated by superpositions of dispersive, single-mode plane waves that each satisfy the 2-D scalar wave equation.

In order to improve the suitability of the Helmholtz approximation for surface waves, the wavefield is usually first filtered around a fixed frequency ω. WEI then proceeds by estimating all spatial and temporal derivatives in eq. (24) given measurements of a passing wavefield made on a dense array. Thereafter the equation can be solved for the phase velocity c_ω, assuming that a single surface wave mode exists in the data. Nevertheless, the series of approximations above degrades the estimates of surface wave velocity.

In acoustic media however, the Helmholtz wave equation may be a reasonable model of wave propagation because the only approximation made in the governing physics is that density is assumed to be locally constant across the array of receivers used to estimate

spatial derivatives in ∇P. To account for a spatial variability in subsurface density, we consider the full acoustic wave equation (eq. 25) in the time domain:

$$\nabla \cdot \left(\frac{1}{\rho(\boldsymbol{x})} \nabla P(\boldsymbol{x}, t) \right) = \frac{1}{\rho(\boldsymbol{x}) c_\omega(\boldsymbol{x})^2} \partial_t^2 P(\boldsymbol{x}, t). \tag{25}$$

The full acoustic wave equation represents the underlying physics that relates phase velocity c_ω and density ρ to dilatational wavefield observations where pressure P is used as wavefield quantity Φ. In acoustic media, eq. (25) captures the full physics whereas it is only an approximation of wave propagation in elastic media. To perform WEI on the basis of the full acoustic wave equation in elastic media, we need to compute the pressure wavefield P from eq. (7) and substitute the resulting potential $\Phi = K_a \nabla \cdot \boldsymbol{u}$ into eq. (10) where $\boldsymbol{u} = \boldsymbol{u}_H$ and $\nabla = \nabla_H$.

Using the foundation of the full acoustic wave equation we set up an inversion process to estimate both velocity and density from gradiometric measurements. We first parametrize the system in order to remove non-linearity in these forward relations. We simplify the form of eq. (25) by introducing parameters $g(\boldsymbol{x})$ and $h(\boldsymbol{x})$ that vary as a function of horizontal position:

$$h(\boldsymbol{x}) = \frac{1}{K(\boldsymbol{x})} = \frac{1}{\rho(\boldsymbol{x}) c_\omega(\boldsymbol{x})^2} \tag{26}$$

$$g(\boldsymbol{x}) = \frac{1}{\rho(\boldsymbol{x})}. \tag{27}$$

The full acoustic wave equation then becomes

$$\nabla g(\boldsymbol{x}) \nabla P(\boldsymbol{x}, t) = h(\boldsymbol{x}) \partial_t^2 P(\boldsymbol{x}, t). \tag{28}$$

We rely on accurate knowledge of second order spatial gradients of pressure which can not be measured directly in the field. We calculate these gradients discretely using finite differences which are based around Taylor series expansions (Curtis & Robertsson 2002). We discretize eq. (28) on a horizontal, regularly spaced receiver grid at the surface (Fig. 2a) using classical central finite differences (FD) after (Geiger & Daley 2003) to approximate the derivatives. Discretizing with the FD method does not require regular grids if we adopt a generalized FD scheme after (Liszka & Orkisz 1980; Huiskamp 1991; Gavete et al. 2003), however in our case receiver spacing Δx and Δy in x- and y-directions, respectively, are constant and equal, and indices i and j define receiver locations, where i ranges from [0,M] and j ranges from [0,N]. We formulate the discretized expression and rearrange the terms isolating the model parameter $g_{i,j}$ that contains information about subsurface density only:

$$\frac{1}{2\Delta x^2} \Big[P_{[0,-]}^n \, g_{[i,j-1]} + P_{[-,0]}^n \, g_{[i-1,j]}$$

$$+ P_{[\pm,\pm]}^n \, g_{[i,j]} + P_{[+,0]}^n \, g_{[i+1,j]} + P_{[0,+]}^n \, g_{[i,j+1]} \Big]$$

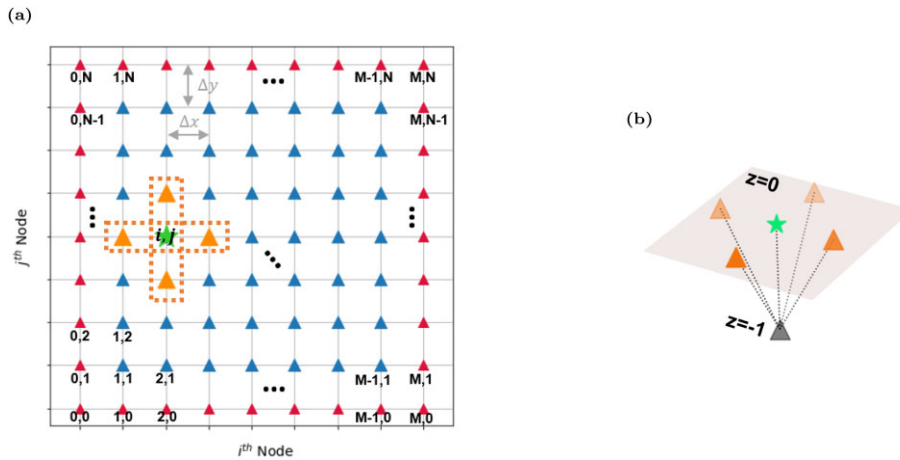$$= h_{[i,j]} \left[\frac{P_{[i,j]}^{n+1} - 2P_{[i,j]}^n + P_{[i,j]}^{n-1}}{\Delta t^2} \right], \tag{29}$$

where $P_{[0,-]}^n$ and $P_{[0,-]}^n$ are written similarly to

$$P_{[0,+]}^n = P_{[i,j+1]}^n - P_{[i,j]}^n \tag{30}$$

$$P_{[+,0]}^n = P_{[i+1,j]}^n - P_{[i,j]}^n \tag{31}$$

and

$$P_{[\pm,\pm]}^n = P_{[0,-]}^n + P_{[-,0]}^n + P_{[0,+]}^n + P_{[+,0]}^n. \tag{32}$$

(a)

(b)

Figure 2. (a) Discretization of wavefield derivatives using a surface receiver grid, shown in plan view on the *x*–*y* plane. Receivers are marked by triangles (internal stations in blue, border stations in red). The grid has N rows in *y*-direction and M columns in *x*-direction. The pressure field *P* is recorded at each receiver position [*i,j*]. The classical second order finite difference stencil of receivers is represented by the cross-shape (orange), using which the second order derivative of the wavefield is estimated at the central point marked by the star symbol (green). (b) shows the corresponding buried receiver (grey) at 1 m below the surface that is used for volumetric gradiometry across the finite difference cross-shaped stencil.

Eq. (29) can be written in matrix form

$$\mathbf{A}\,\mathbf{g}^{est}\ =\ \mathbf{d}, \tag{33}$$

where matrix $\mathbf{A}$ has dimensions $[R \times R \times n_t]$ with R being the number of parameters over the receiver grid ($R = M \times N$) and n_t the number of data in the time-series. $\mathbf{A}$ contains purely observed data consisting of the pressure differences (eqs 30–32) and is banded and square $[R \times R]$ for each time step n in the time-series of the signal. Vector $\mathbf{g}^{est} = [g_{[0,\,0]}, g_{[1,\,0]},..., g_{[M,\,N]}]^T]$ is the parameter vector of dimension $[R \times 1]$ to be estimated, and $\mathbf{d}$ is an observed data vector of dimension $[R \times n_t]$ that contains time derivatives of the recorded pressure field $P_{i,j}$ multiplied by terms $h_{i,j}$ (right-hand side of eq. 29). Equally accurate calculations of derivatives at the corners and boundaries of the array are not possible since neighbouring receivers are not available in all directions so the full cross-shaped finite difference stencil (Fig. 2) can not be used and is depleted to a stencil formed by two or three adjacent stations only. We therefore introduce a weighting matrix $\mathbf{W}$ that gives less weight to information from corner and boundary points of the receiver grid which are likely to provide less accurate constraints than the internal receivers. For corner and border receivers we chose a weighting factor very close to zero to minimize the impact on results while still maintaining the invertibility of matrix $\mathbf{A}$. Consequently, density estimates are evaluated only at internal receivers.

Since the density information is contained in both parameter vector $\mathbf{g}^{est}$ and the vector $\mathbf{d}$ through parameter vector $\mathbf{h} = [h_{[0,\,0]}, h_{[1,\,0]},..., h_{[M,\,N]}]^T]$, prior information is given in the form of an initial reference model for $\mathbf{h}$ which we call $\mathbf{h}^{init}$:

$$\mathbf{h}^{init}\ =\ \frac{1}{\rho_{init}\,c_{\omega,init}}. \tag{34}$$

So as not to bias the inversion towards a heterogeneous solution, we chose a homogeneous reference for density ρ_{init}. The reference model $c_{\omega,init}$ for phase velocity is obtained from an initial wave equation inversion using the standard scalar Helmholtz wave equation formulation (24) following the methods of De Ridder & Biondi (2015) and Cao *et al.* (2020). To stabilize the inverse problem we

introduce generalized Tikhonov regularization:

$$[\boldsymbol{W}\boldsymbol{A} + \Theta_d\boldsymbol{I}]\,\boldsymbol{g}^{est}\ =\ [\boldsymbol{d} + \Theta_d\boldsymbol{g}^{init}]. \tag{35}$$

Damping term Θ_d controls how strongly the solution is drawn towards the homogeneous reference model $\boldsymbol{g}^{init}$ and has the same dimensions as matrix $\boldsymbol{A}$. We then find the least-squares solution for parameters $\boldsymbol{g}^{est}$ that contain the density information

$$\boldsymbol{g}^{est}\ =\ \left[\Sigma_{n=1}^{n_t}\left(\hat{A}_n^T\hat{A}_n\right)^{-1}\hat{A}_n^T\right]\left[\Sigma_{n=1}^{n_t}\hat{d}_n\right], \tag{36}$$

where $\hat{A} = [\boldsymbol{W}\boldsymbol{A}, \Theta_d\boldsymbol{I}]^T$ and $\hat{d} = [\boldsymbol{d}, \Theta_d\boldsymbol{g}^{init}]^T$. After one iteration solving for $\boldsymbol{g}^{est}$, we obtain a first approximation to density that we note $\boldsymbol{g}'$. Substituting this density approximation into eq. (25), we estimate phase velocity using gradiometric methods where we write the discrete finite difference form of eq. (25) in terms of parameter $\boldsymbol{g}'$ and estimate the phase velocity via linear regression similarly to De Ridder & Biondi (2015):

$$\frac{1}{2\Delta x^2}\left[g'_{[0,-]}P^n_{[i,j-1]} + g'_{[-,0]}P^n_{[i-1,j]} - g'_{[\pm,\pm]}P^n_{[i,j]}\right.$$
$$\left. + g'_{[0,+]}P^n_{[i,j+1]} + g'_{[+,0]}P^n_{[i+1,j]}\right]c^2_{\omega,[i,j]}$$
$$=\left[\frac{P^{n+1}_{[i,j]} - 2P^n_{[i,j]} + P^{n-1}_{[i,j]}}{\Delta t^2}\right], \tag{37}$$

where $g'_{[-,0]}$ and $g'_{[0,-]}$ are written similarly to

$$g'_{[+,0]} = \frac{g'_{[i+1,j]}}{g'_{[i,j]}} + 1 \tag{38}$$

$$g'_{[0,+]} = \frac{g'_{[i,j+1]}}{g'_{[i,j]}} + 1 \tag{39}$$

and

$$g'_{[\pm,\pm]} = g'_{[0,-]} + g'_{[-,0]} + g'_{[+,0]} + g'_{[0,+]}. \tag{40}$$

In matrix form, eq. (37) can be written

$$\boldsymbol{J}'\,\boldsymbol{m}'\ =\ \boldsymbol{d}', \tag{41}$$

where $\mathbf{m}' = [c^2_{\omega,[0,0]}, c^2_{\omega,[1,0]}, ..., c^2_{\omega,[M,N]}]^T$ is the parameter vector of dimension $[R \times 1]$, $\mathbf{d}'$ is an observed data vector of dimension $[R \times n_t]$ that contains time derivatives of the recorded pressure field and coefficient matrix $\mathbf{J}$ of dimensions $[R \times R \times n_t]$ contains knowledge about the pressure wavefield gradients and density gradients from the full acoustic wave equation formulation. In the case of real data, where amplitude differences in the wavefield due to site effects or difference in sensors can impact the data, it might be necessary to impose the condition that medium parameters should not vary rapidly as a function of space (De Ridder & Biondi 2015). This can be achieved by penalizing the second order spatial derivatives in the form of a regularization term. For the purpose of this paper, where we analyse synthetic data only and the problem is well constrained, eq. (37) is solved by linear regression with a mean squared error cost function, that is non-regularized least-squares WEI. Information about density obtained from eq. (36) and the updated phase velocity estimates obtained by solving eq. (37), provide an updated estimate of $\mathbf{h}$ denoted $\mathbf{h}'$:

$$\mathbf{h}' = \frac{\mathbf{g}'}{\mathbf{m}'}. \tag{42}$$

and $\mathbf{g}^{init}$ is updated by $\mathbf{g}'$. We proceed to perform several iterations of solving eqs (36) and (37) until we observe convergence towards a stable estimate of $\mathbf{g}'$. In the following, we analyse this methodology for acoustic media, then test its performance in elastic media.

3.2 Volumetric arrays

To estimate density with volumetric gradiometry in an elastic medium, a 2-step procedure is implemented. First, we discretize eq. (18) with finite differences on the volumetric array (Fig. 2b) and estimate body wave velocities with linear inversion techniques based on the free surface methodology described in Curtis & Robertsson (2002). We use a standard non-regularized, least-squares minimization technique to estimate v_S' and v_P'. Secondly, we discretize left- and right-hand sides of eq. (23) with classical finite differences and substitute the estimated body wave velocities v_S' and v_P' obtained from WEI:

$$\left[\partial^2_t \, u_z + v^2_P{}' \underbrace{\left[-\frac{2}{\Delta z}[\partial_z u_z]_{fd} + \nabla^2_H u_z \right] - 2v^2_S{}' \nabla^2_H u_z}_{LHS} \right]_{[i,j,0]}$$
$$= \frac{1}{\rho_{[i,j,0]}} \underbrace{\left[\frac{1}{\Delta z}\left(2 - \frac{4v^2_S{}'}{v^2_P{}'}\right)P \right]_{[i,j,0]}}_{RHS} \tag{43}$$

where,

$$LHS_{[i,j,0]} = \frac{u^{n+1}_{z[i,j,0]} - 2u^n_{z[i,j,0]} + u^{n-1}_{z[i,j,0]}}{\Delta t^2} - \frac{2}{\Delta z}v^2_{P[i,j,0]}{}'\left[\frac{u_{z[i,j,-1]} - u_{z[i,j,0]}}{\Delta z}\right]$$
$$+ (v^2_{P[i,j,0]}{}' - 2v^2_{S[i,j,0]}{}')\frac{u^n_{z[i,j-1,0]} + u^n_{z[i-1,j,0]} - 4u^n_{z[i,j,0]} + u^n_{z[i+1,j,0]} + u^n_{z[i,j+1,0]}}{\Delta x^2} \tag{44}$$

$$RHS_{[i,j,0]} = \frac{1}{\Delta z}\left(2 - \frac{4v^2_{S[i,j,0]}{}'}{v^2_{P[i,j,0]}{}'}\right)P_{[i,j,0]} \tag{45}$$

which enables density to be estimated via linear regression at each receiver position $[i,j,0]$ at the surface:

$$LHS_{[i,j,0]} = \frac{1}{\rho_{[i,j,0]}} RHS_{[i,j,0]}. \tag{46}$$

4 SYNTHETIC TESTS

By using wavefield gradiometry we aim to image the shallow subsurface in as much detail as possible. With the following synthetic study we wish to examine the role of density in enhancing or obscuring our resolution of lateral heterogeneities.

We use the 3-D wavefield modelling software Salvus (Afanasiev *et al.* 2019) to produce accurate synthetic acoustic and elastic wavefield recordings in 3-D heterogeneous media. The wavefield is recorded at the surface over a 40×40 receiver grid in the middle of the domain. As a rule of thumb in gradiometry, the wavefield should be sampled at spatial points spaced a maximum of around 12 per cent of the minimum wavelength apart, in order to obtain an accuracy of 10 per cent in first order spatial derivatives (Langston 2007a). Analogous error calculations for second order derivatives suggest that for a same level of accuracy receivers must be spaced at a maximum of 24 per cent of the minimum wavelength (Appendix A); in other words for the same receiver spacing, second order derivatives are less prone to large finite difference errors than first order derivatives. With a spacing of 2 m and a minimum medium velocity of 1550 m s^{-1}, this allows frequencies up to 180 Hz to be used with reasonable accuracy. All wavefields are recorded for a time interval of 3 s at a temporal sampling rate of 0.3 ms. A buried receiver is placed 1 m below every receiver on the surface array for volumetric gradiometry.

Relevant depth slices and plan view maps of the true acoustic *P*-wave velocity and density model are shown in Fig. 3. The velocity heterogeneity of the top layer follows a sine function in the *x*-direction at a wavelength of approximately 113 m. The density structure has a wavelength of 88 m and is rotated by 90° with respect to the velocity structure in order that we can clearly identify successful estimates of each parameter without concerns that we are actually estimating only their correlation. The rotation of the orientation of density heterogeneities relative to those in velocity should also reveal whether the estimated density structure contains artefacts caused by velocity heterogeneity and vice versa. Layer 1 is 50 m thick and velocities span the range 1550 to 2300 m s^{-1}, densities span 1200–2000 kg m^{-3}, while the deeper layer has a homogeneous velocity of 2700 m s^{-1} and density of 2240 kg m^{-3}. The receiver array spans an area of 78×78 m^2 and captures at least half a wavelength of the heterogeneity in both velocity and density structures (Figs 3b and d). Elastic models are constructed analogously to Fig. 3 with an additional *S*-wave velocity model related to *P*-wave velocity by a Poisson ratio of 0.25.

To test the performance of WEI for simulated ambient noise, five isotropic sources are placed on a circle around the receiver array at a radius of 290 m from the midpoint. They fire Ricker wavelet signatures with different central frequencies ranging from 4.5 to 16 Hz at random time intervals but with the same amplitude to examine whether WEI is robust against waves of overlapping frequency. The sources fire close to the surface at 10 m depth to ensure that the dominant wave energy travels along the surface, allowing the assumption that the pressure gradient in *z*-direction is small compared to horizontal directions. The increasing velocity with depth in the model ensures that the waves are dispersive as in the true Earth's subsurface.

In addition to the proof-of-concept synthetic model where density structure is orthogonal to the velocity structure, which is discussed in the main body of the paper, we examine models that resemble natural borders between geological units more closely in Appendix D. Two true density models whose structure oscillates in parallel with the velocity structure of Figs 3(a) and (b) are analysed for the acoustic data case. In Fig. D1(a) the density gradients follow the same sine curve as the velocity structure and are directly aligned with the velocity gradients (Fig. D1b), whereas the density and velocity in
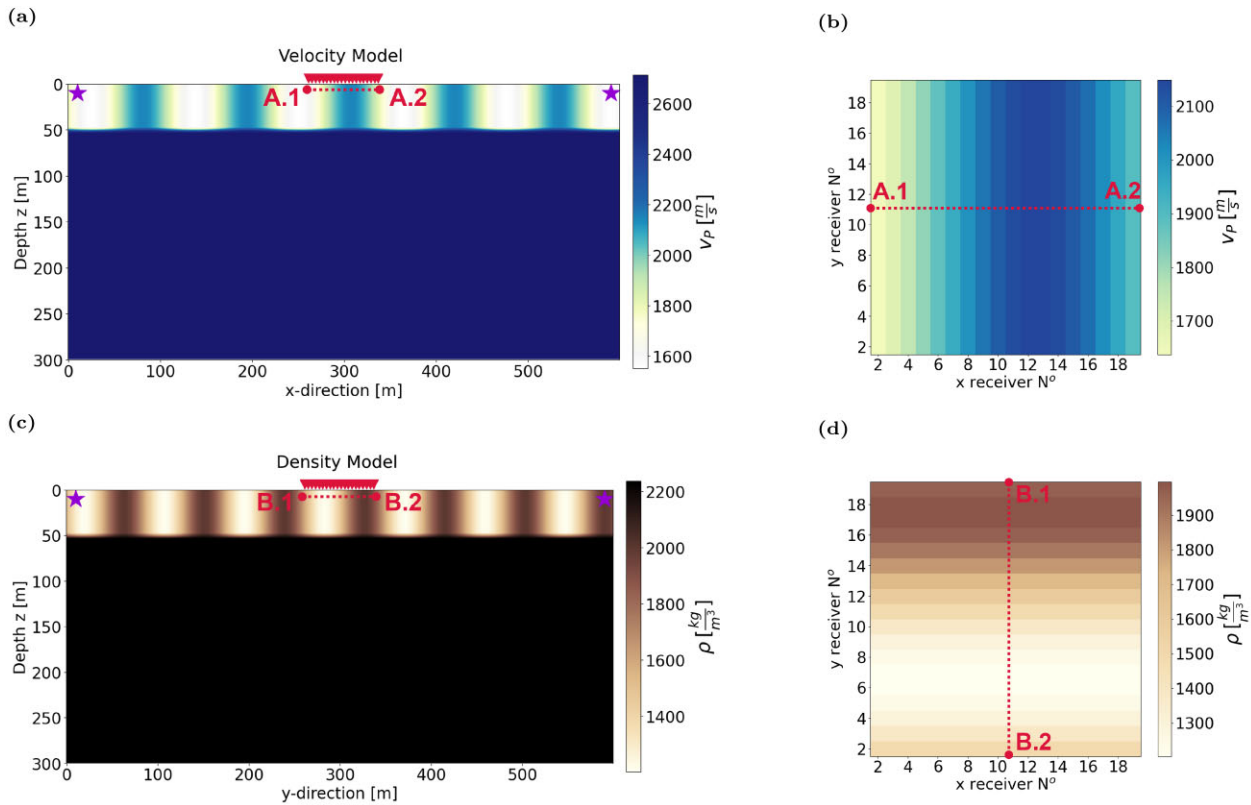
Figure 3. (a) Acoustic velocity model cross-section in *xz*-plane. Source locations relative to the receiver array are indicated by stars. Receiver groups marked by red triangles highlight the location of one line of 40 receivers at the surface and their corresponding buried receiver positioned at 1 m depth below. The total array spans an area of 78×78 m^2 spaced at 2 m intervals across the range [261, 339] m in both *x*- and *y*-directions. For gradiometry relying exclusively on the surface array, derivatives are calculated over a decimated receiver grid spaced at 4 m, whereas all surface receivers at 2 m intervals are used to perform volumetric gradiometry. All plan views showing model parameters are represented on the decimated grid at 4 m receiver spacing. (b) 2-D *xy*-plan view map of the section of the true velocity model spanned by the internal receivers of the surface array. Depth boundary from layer 1 to layer 2 does not correspond to a step function change but a linear increase within the model cell that transitions between properties from the shallower layer to the deeper layer. (c) Density model depth cross-section in *yz*-plane. (d) 2-D *xy*-plan view map of the section of the true density model spanned by the internal receivers of the surface array. For the pressure signals in Figs 4(a) and (b), a constant density model of 1600 kg m^{-3} is used instead for the top layer (Appendix B, Fig. B1). Elastic runs are performed with the same velocity and density structure and an additional shear-wave velocity field. Acoustic and elastic forward models have slightly different meshing criteria due to their respective minimum model velocities.

Figs D2(a) and (b) both also vary in the *x*-direction but are spatially shifted with respect to each other.

5 DENSITY FINGERPRINT

5.1 Free surface arrays

Sensitivity to relative density gradients in the full acoustic wave equation

The full acoustic wave eq. (25) can be written in the form of the Helmholtz wave equation and a source term containing relative density gradients $\nabla \rho(\boldsymbol{x})/\rho(\boldsymbol{x})$ acting on pressure gradients $\nabla P(\boldsymbol{x}, t)$:

$$\nabla^2 P(\boldsymbol{x}, t) - \frac{1}{c_\omega(\boldsymbol{x})^2} \partial_t^2 P(\boldsymbol{x}, t) = \frac{\nabla \rho(\boldsymbol{x})}{\rho(\boldsymbol{x})} \cdot \nabla P(\boldsymbol{x}, t). \tag{47}$$

Relative density gradients influence pressure gradients whenever a spatial density gradient $\nabla \rho(\boldsymbol{x})$, that is, a laterally heterogeneous density structure, exists. Otherwise the term on the right-hand side of eq. (47) becomes zero.

To illustrate the role that relative density gradients play in influencing wavefields we compare the second-order spatial pressure gradient terms in Fig. 4 for a model in which density varies (Fig. 3) to one in which density is fixed at the average value of the former model (Appendix B, Fig. B1). The spatial pressure gradients are expressed as

$$\nabla^2 P(\boldsymbol{x}, t) \tag{48}$$

for the Helmholtz eq. (24) and

$$\rho(\boldsymbol{x}) \nabla \cdot \left(\frac{1}{\rho(\boldsymbol{x})} \nabla P(\boldsymbol{x}, t) \right) \tag{49}$$

for the full acoustic eq. (25). For simplicity of notation, we drop the indication of space and time dependencies of density ρ and pressure P hereafter. In variable density media, terms (48) and (49) have quite different discretized finite-difference coefficients as shown in Table 1. In the Helmholtz case, classical discretization coefficients for second order derivatives are used, whereas ratios of density from neighbouring receiver stations dominate the discretization coefficients in the full acoustic case (eqs 37–40). If the pressure field passes through a homogeneous medium, the coefficients in the full

(a)

(b)

(c)

(d)
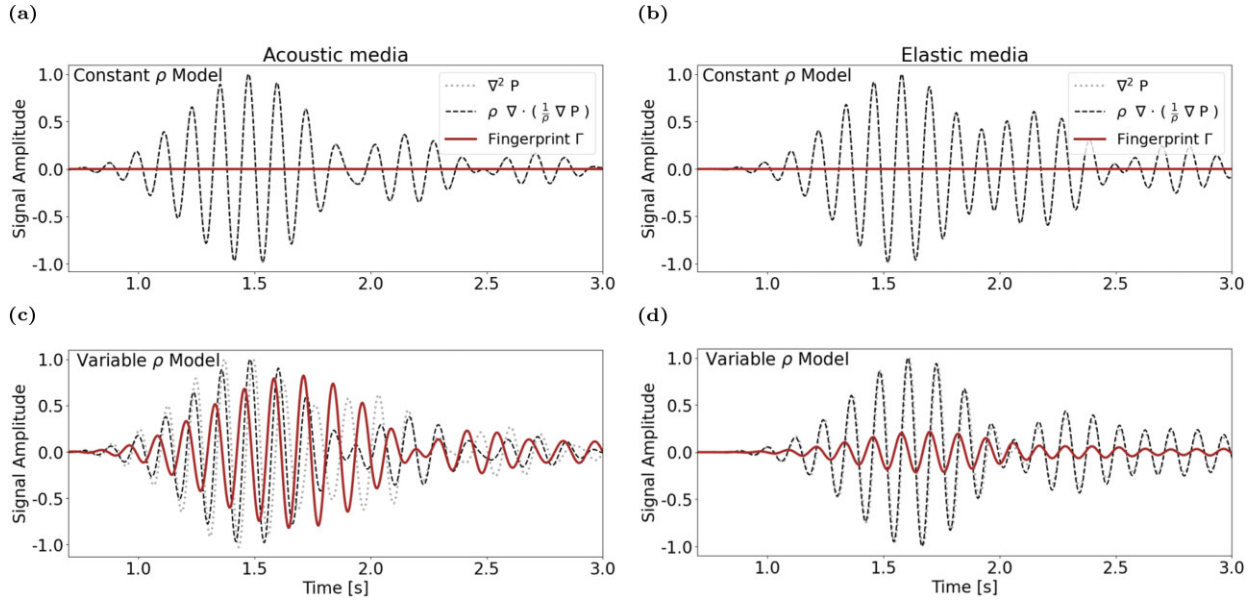
Figure 4. Effect of density gradients in 3-D acoustic (a and c) and elastic media (b and d). Panels (a) and (b) show the discretized Helmholtz (dotted grey) and full acoustic (dashed black line) normalized spatial gradients at receiver [13,13] for a constant acoustic and elastic density model (Appendix B, Fig. B1) respectively. The difference between Helmholtz and full acoustic gradients (solid red line) shows that constant density has no influence on the measured wavefield. Panels (b) and (d) show the same information for a heterogeneous density model (Figs 3c and d) in acoustic and elastic media, respectively. The difference between Helmholtz and full acoustic gradients contains the signal generated by the density gradient in *y*-direction. The influence of the density gradient can clearly be distinguished (solid red line). In this example, the wavefield is filtered between 7 and 9 Hz.

Table 1. If divided by receiver spacing Δx^2, the presented values correspond to finite difference discretization coefficients on a regular grid (Fig. 2) for second order spatial pressure gradients in Helmholtz (24) and full acoustic (25) equations, respectively. Helmholtz coefficients correspond to the classical central finite difference discretization values. Full acoustic coefficients are dependent on density ratios $\boldsymbol{g}'$ (eqs 38–40) of neighbouring receivers.

	$[j-1]$	$[i-1]$	$[i,j]$	$[i+1]$	$[j+1]$
Helmholtz	1	1	-4	1	1
Full acoustic	$\frac{1}{2}\boldsymbol{g}'_{[0,-]}$	$\frac{1}{2}\boldsymbol{g}'_{[-,0]}$	$\frac{1}{2}\boldsymbol{g}'_{[\pm,\pm]}$	$\frac{1}{2}\boldsymbol{g}'_{[+,0]}$	$\frac{1}{2}\boldsymbol{g}'_{[0,+]}$

acoustic case reduce to the Helmholtz coefficients since ratios of adjacent density values are equal to 1: the phase velocity estimates are thus identical in this case regardless of which equation is used for WEI. Whenever the densities between neighbouring receiver stations vary, the full acoustic coefficients contain density ratios not equal to 1 and an effect on the phase velocity estimate is expected depending on whether the Helmholtz or the full acoustic wave equation is used as a basis for WEI.

This behaviour of the spatial gradients becomes obvious in both acoustic (Figs 4a and c) and elastic (Figs 4b and d) media. In the homogeneous model, Helmholtz and full spatial gradients are the same, resulting in no difference between them (Figs 4a and b). In the model with variable density we observe a clear change in wave amplitude and a phase shift between the two spatial gradient expressions which is prominent between recording times 1 and 2 s in the acoustic case (Fig. 4c). Density gradients therefore create a clearly distinguishable fingerprint in measureable wavefield quantities (Figs 4c and d), where the fingerprint $\boldsymbol{\Gamma}$ is defined as the difference between normalized spatial gradients:

$$\boldsymbol{\Gamma} = \left[\rho \nabla \cdot \left(\frac{1}{\rho}\nabla P\right)\right] - [\nabla^2 P] = \frac{\nabla \rho}{\rho} \cdot \nabla P. \quad (50)$$

In the synthetic model, density varies exclusively in the *y*-direction, so $\partial_x \rho = 0$ and $\boldsymbol{\Gamma}$ reduces to the form:

$$\boldsymbol{\Gamma} = \frac{1}{\rho} \partial_y \rho \, \partial_y P. \quad (51)$$

The difference between Helmholtz and full acoustic spatial gradients is less pronounced in elastic media, even though underlying density gradient values are the same in both acoustic and elastic models. Nevertheless, neglecting variability in the density structure in either acoustic or elastic media results in gradients that are not representative of the propagation medium. This causes the phase velocity to be either over- or underestimated by WEI when using the Helmholtz equation in a variable density medium.

5.2 Volumetric arrays

Sensitivity to density in the free surface, full elastic wave equation

The linear equation derived from the vertical component of the Lax–Wendroff corrected full elastic wave equation puts constraints on density directly. Eq. (46) shows that density linearly relates the temporal and spatial derivatives of displacement to the pressure

term. In Fig. 5 it becomes clear that the left- and right-hand sides of eq. (46) are related by a scaling factor. By fitting a regression line with the slope of the inverse of true density in the heterogeneous forward model, a coefficient of determination R^2 equal to 1 is obtained suggesting that the scaling factor between left- and right-hand sides corresponds to the density of the medium. Fig. 5(b) shows that residuals are essentially zero between left-hand and right-hand sides of eq. (46) if the true density is substituted. The same is observed in homogeneous media.

6 INVERSION RESULTS

We now present results from the iterative inversion process for density and phase velocity using simulated ambient noise. In Section 6.1.1 we investigate the performance of density estimation in acoustic media at a central frequency of 8 Hz where the wavefield data is filtered with a narrow bandpass in the range 7–9 Hz. We then show how that density information improves the accuracy of phase velocity estimates based on WEI of the full acoustic wave equation, and how random noise impacts the robustness of these estimates. We then investigate the quality of density inversion over a broader frequency range from 4 to 14 Hz and the impact that full WEI has on estimates of phase velocity dispersion curves. In Section 6.1.2, we discuss the density estimated in elastic media using acoustic equations for WEI and the same iterative inversion workflow. Misfit functions are then presented to illustrate trade-offs between density and phase velocity in both acoustic and elastic media (Section 6.1.3). Thereafter, we show density results in elastic media obtained by gradiometric linear regression using the full elastic wave equation at the free surface (Section 6.2). An overview of the structure of this results section summarizing the data types, array configurations and governing equation assumed in the inversion methods is given in Table 2.

6.1 Free surface arrays

6.1.1 Acoustic data

Density estimation

Fig. 6(a) shows the density inversion results as a mean over all cross sections in x (Fig. 6a, left-hand panel) and y-direction (Fig. 6a, right-hand panel). Corresponding lateral relative y- and x-gradients in density are depicted in Fig. 6(b) in the left- and right-hand column, respectively. Without damping, there is no constraint on the absolute value of the density. Hence, the inversion process is quite sensitive to different initial damping parameters Θ_d. As a rule of thumb, setting the initial damping parameter at 10 per cent of the mean amplitude of all recorded pressure signals stabilized our inversions. The mean value over the true density model is fed to the inversion as the initial homogeneous reference model ρ_{init}.

We clearly see the effect of the damping term in the first iteration where the inverted density estimate is skewed towards the initial reference model. After the initial iteration we decrease the damping parameter by a factor of 10 and keep it constant for a total of 100 iterations. Lowering the damping parameter gives less weight to the reference model. Tests showed that the inversion process is only sensitive to the initial damping parameter: decreasing the damping parameter further after the initial stabilization phase did not have an effect on the final result, but it allowed the inversion to converge more quickly towards a minimum misfit solution. After only 10

iterations of alternately updating velocity and density, the density estimates approximate the true solution fairly well and remain stable over subsequent iterations. The initial spiky character observed in the x-direction might arise because we did not impose any smoothness constraints on the inversion. The logarithm of the data misfit vector δ_d of dimension $[R \times 1]$

$$\delta_d = \frac{\Sigma_{n=1}^{n_t} \left(\boldsymbol{J}'_n \, \boldsymbol{m}' - \boldsymbol{d}_n \right)^2}{n_t} \tag{52}$$

for the predicted model at each iteration is shown in Fig. 6(c) and is used to determine whether the iteration delivers satisfactory results. After the initial iteration the logarithm of the full acoustic misfit of -7.0 is comparable to the Helmholtz misfit level at a value of -6.1. From there, the data misfit monotonically decreases with each iteration. In the first 10 iterations, the logarithmic misfit decreases rapidly from -7.0 to -13.2 at iteration 10. After 12 iterations the logarithm of the misfit remains almost constant around a value of -13.5 and only improves marginally to -13.9 until the inversion is stopped at iteration 100.

The steep drop in misfit at iteration 10 correlates well with the improvement in the relative parameter error on the relative density gradient in the y-direction. The relative error of parameter p at each location i,j is defined as the difference between the absolute values of true and estimated values $|p|^{\text{true}}$ and $|p|^{\text{estimate}}$ divided by the true values

$$|Error|_{i,j} = 100 \left| \frac{|p|_{i,j}^{\text{true}} - |p|_{i,j}^{\text{estimate}}}{|p|_{i,j}^{\text{true}}} \right|, \tag{53}$$

where in this instance, parameter p stands for the relative x- or y-density gradients $\partial_x \rho / \rho$ and $\partial_y \rho / \rho$, respectively, but can stand for any other estimated quantity. In the case where the true value in eq. (53) is equal to 0, the denominator is replaced by 1.

The density gradient result with minimum parameter error in x-direction is achieved at iteration step 21. The slight increase in parameter error in density thereafter is likely to originate from the velocity updates dominating the misfit evolution. Velocity has a much stronger effect than the density since it appears squared in the full acoustic wave equation. We showed in Fig. 4 that in a medium with homogeneous density the spatial gradient expressions from the Helmholtz and the full acoustic equation are identical and so phase velocity estimates remain unaffected by homogeneous densities across the array. Since density is constant in the x-direction, the true phase velocity is only dependent on density structure in the y-direction. Given the poor constraints on density in the x-direction the mean estimate on the density gradient in x-direction deviates, if only slightly (± 0.15 per cent), from the true value of zero (Fig. 6b). This introduces artefacts in the phase velocity estimates which in turn impairs density estimates throughout the iterative process. Nevertheless, in our experiments the data misfit minimum does tend to indicate when parameter estimates are most accurate. Cross-talk between density and velocity appears to be weak because the density structure of the true model could be reconstructed with reasonable accuracy without major artefacts (Fig. 6).

Relative density gradient results for models with parallel spatial gradients (i.e. density structure varying in the same directions as the velocity structure) are shown in Appendix D (Figs D1c and D2c) and could also be reconstructed without a significant increase in cross-talk compared to the models with density and velocity spatial gradients orthogonal to each other. Misfits are higher by two to three orders of magnitude but still suggest a good agreement with
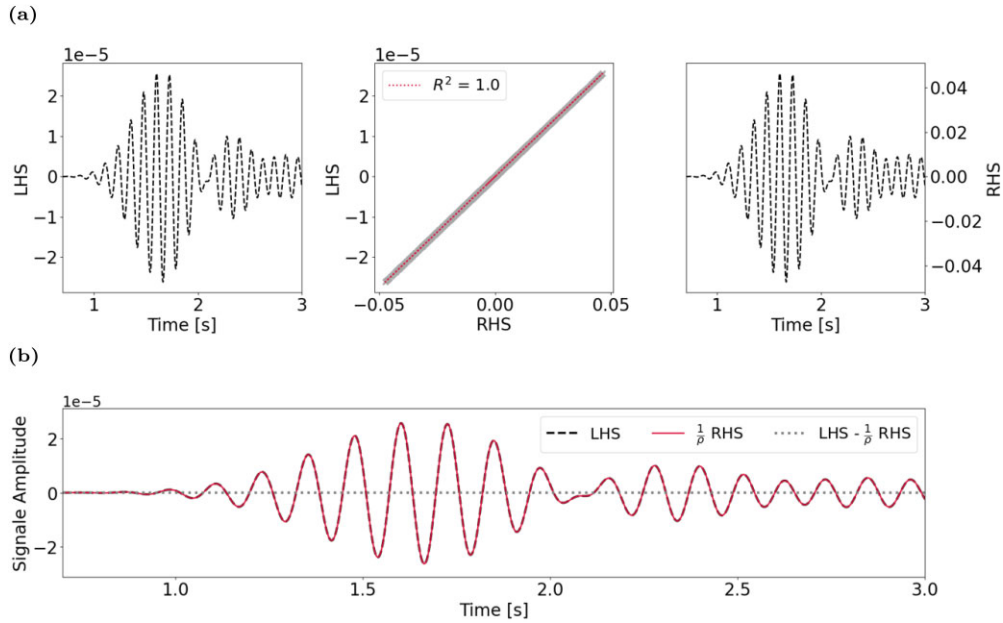
Figure 5. Role of density at the free surface of 3-D elastic media [heterogeneous forward model (Fig. 3)] shown at the example receiver at location [13,13]. The wavefield is filtered around a central frequency of 8 Hz with a bandpass of 2 Hz. Panel (a) shows the waveform of the discretized left-hand side (left-hand panel) and right-hand side (right-hand panel) of eq. (46) when true velocity model parameters are used. The middle panel in (a) shows a scatter plot of left- and right-hand data with a regression line of a slope corresponding to the inverse of true density at receiver [13,13]. R^2 is the coefficient of determination defining the goodness of fit of the regression line and the data. Panel (b) shows the residuals (LHS-$1/\rho$ RHS) between left- and right-hand side of eq. (46) if the true model density is used.

Table 2. Overview of the WEI approaches that are used in the Inversion Results section. For the inversion method based on free surface arrays (Fig. 2a) and volumetric arrays (Fig. 2b), used to produce the results, the reader can refer to Sections 3.1 and 3.2, respectively. For free surface arrays, the governing equation used to estimate density is the full acoustic wave eq. (25): density inversion with surface arrays using full acoustic WEI is tested on synthetic data from both acoustic and elastic media. For volumetric arrays, density is obtained using a modified version of the full elastic wave equation at the free surface (eq. 43) in which both vertical particle velocity and pressure appear.

Array type	Synthetic medium	Equation used for WEI
Free surface (Section 6.1)	Acoustic (Section 6.1.1) Elastic (Section 6.1.2)	Full acoustic (from Section 3.1, eq. 25)
Volumetric (Section 6.2)	Elastic (Section 6.2.1)	Modified full elastic free surface (from Section 3.2, eq. 43)

the data (Figs D1d and D2d); also the evolution of the mean error on the relative density gradients is comparable to the model with orthogonal density and velocity structures.

As discussed in Section 5, the inversion is predominantly sensitive to relative changes in density $\nabla\rho/\rho$, where $\nabla\rho$ corresponds to the gradient of density at a central point $\rho = \rho_{i,j}$ over the finite difference stencil (*cf.* Fig. 2), and is less sensitive to the absolute values $\nabla\rho$ (Fig. 7). Fig. 7 shows that the minimum misfit estimate of the local density gradient in the *y*-direction is typically within ± 10 per cent of the true value for relative density changes larger than 0.5 per cent over the width of the spatial finite difference stencil. The accuracy of estimates decreases for weak relative changes below 0.5 per cent. Estimates of absolute values may be biased depending on which initial density reference model is fed to the first iteration of the inversion. Results in Fig. 6(a) could successfully reconstruct absolute density values due to an appropriate choice of starting model ρ_{init}. If the initial guess of bulk density varies more significantly from the true values, the absolute estimates are under-

or overestimated according to the input starting model (Fig. 7a, left-hand panel) because the inversion fits the relative changes in density ratios (Fig. 7a, right-hand panel) as becomes obvious from eq. (47). By reconstructing relative density changes, the results are unbiased by the choice of initial density model ρ_{init} (Fig. 7a, right-hand panel). The results of relative density gradients for each local receiver position over the entire grid are shown in Fig. 8 as 2-D plan view maps.

*Effect of density gradient on phase velocity estimates*

We now show the extent to which the estimated density structure influences the accuracy of phase velocity maps. Fig. 9(a) shows the phase velocity map estimated using the same data as above, but with the Helmholtz wave equation, so without taking density into account in the formulation of wave propagation. Fig. 9(b) shows phase velocity estimates based on the full acoustic wave equation at iteration 100 where the data misfit is minimal.
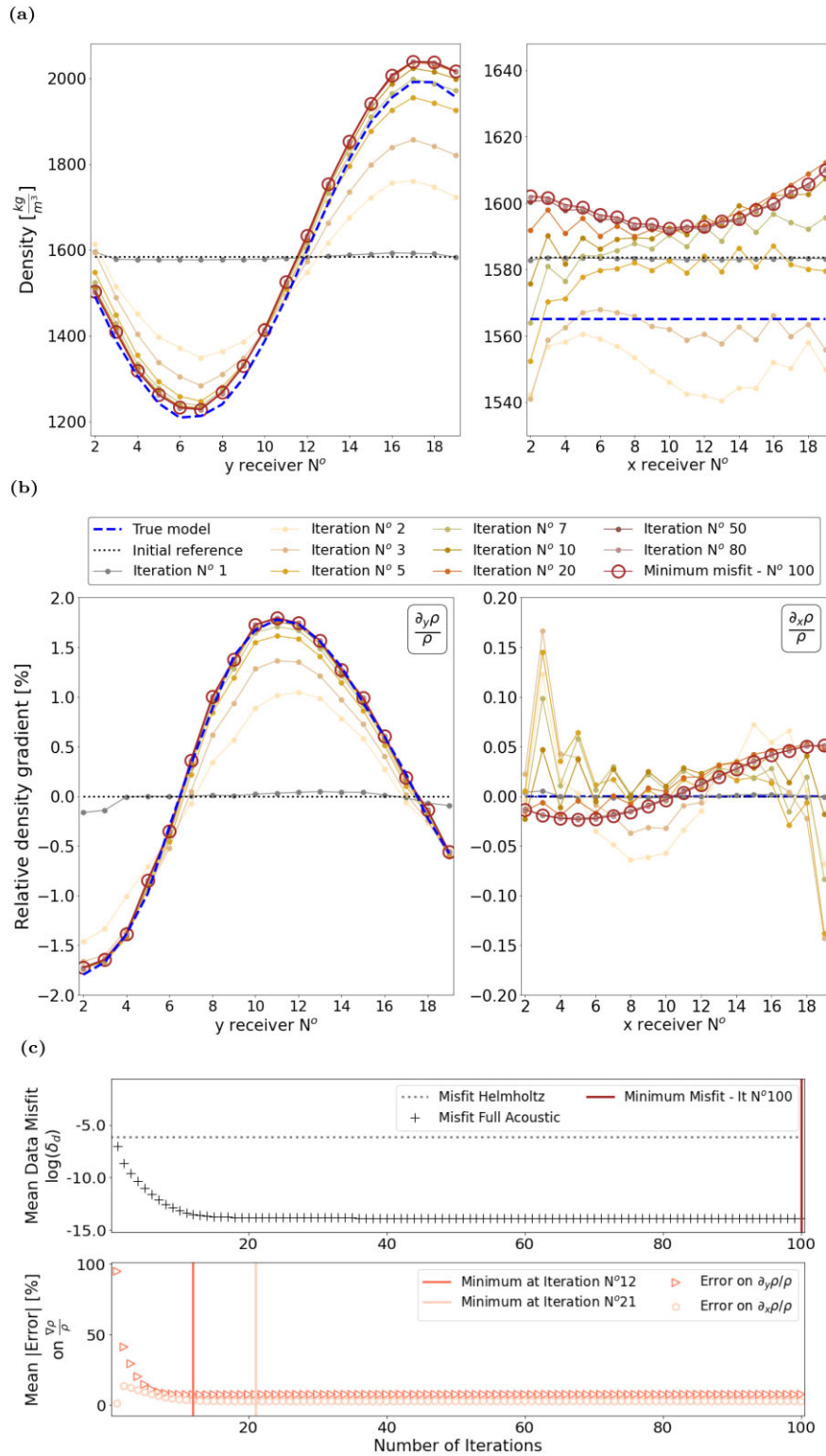
Figure 6. Inversion result for a wavefield filtered to include frequencies in the range of 7–9 Hz. Only the results for the internal receivers 2–19 are displayed, as boundary stations need to be disregarded for finite difference estimates. (a) Mean value of inverted density results over all cross-sections in *x*-plane (left-hand panel) and *y*-plane (right-hand panel) showing the evolution of inverted density results at selected stages during 100 iterations. True model is depicted as dashed dark blue line and initial model as dotted black line. The minimum misfit result at iteration 100 is highlighted by red circles. (b) Relative density gradients $\nabla \rho / \rho$ of (a) in *y*- and *x*-direction, respectively. (c) Logarithm of the mean data misfit evolution for the full acoustic wave equation (black crosses) over all internal receivers (upper row) and corresponding mean parameter error on *x*- and *y*-relative density gradients over all internal receivers (lower row) spanning over 100 iterations. Their respective minimum value positions are marked by vertical lines in red for minimum misfit at iteration 100, dark orange and light orange at iteration 12 and 21 for minimum parameter error on relative density *y*- and *x*-gradients. As a reference, the misfit achieved with linear regression based on the Helmholtz equation is shown by the dotted grey line. The minimum mean parameter error is evaluated only after the initial iteration.
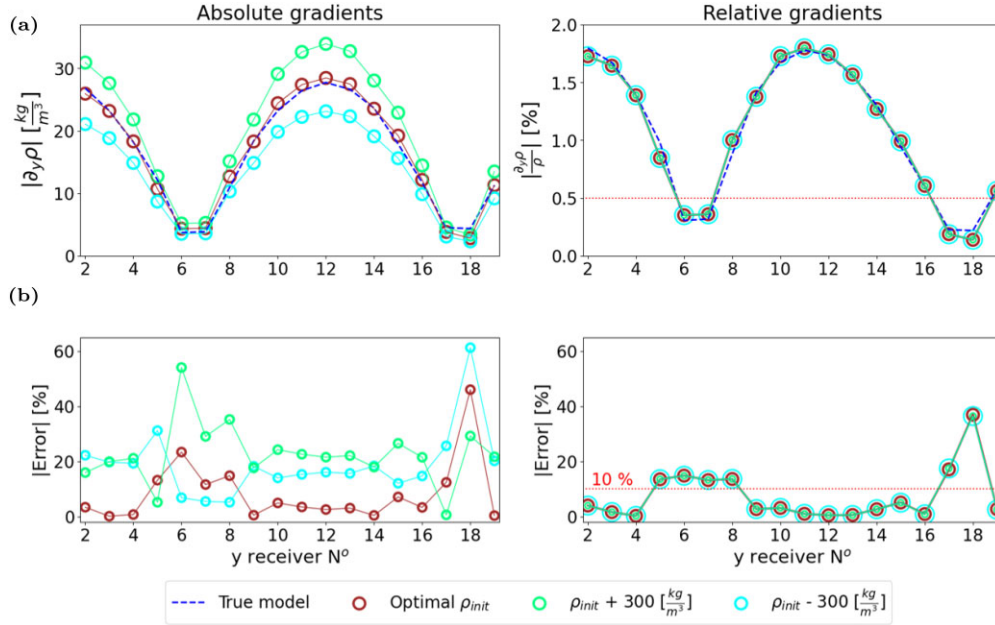
Figure 7. Impact of initial density reference model ρ_{init} on inversion results of (a) absolute density y-gradients $\partial_y\rho$ (left-hand panel) and relative density y-gradients $\partial_y\rho/\rho$ (right-hand panel). Their respective errors (eq. 53) are depicted in (b). Results from an optimal ρ_{init} starting model (red circles) correspond to the estimates in Fig. 6(a) where ρ_{init} is the mean bulk density of the true model (dashed dark blue line). Results for a less well informed initial reference model with higher mean bulk density (green circles) and lower mean bulk density (light blue circles) are shown for comparison.
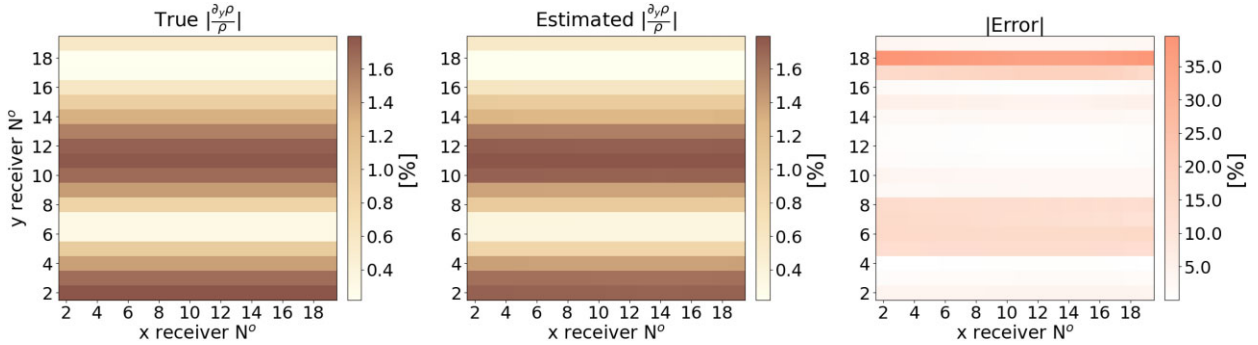
Figure 8. Plan view of (left-hand panel) true model and (middle panel) inversion results for absolute values of relative density gradients in y-direction $\partial_y\rho/\rho$ at iteration 100. The corresponding parameter error (eq. 53) is shown in the right-hand panel.

By visually comparing these maps to the true velocity structure (Fig. 3b) it is obvious that the Helmholtz approach fails to reproduce the relative structure of the subsurface velocity pattern. By contrast, the results obtained by WEI of the full acoustic wave equation yield an improved estimate of the velocity structure that is much closer to the true model in terms of relative structural features. This observation is reflected in the much lower misfit values obtained for the full acoustic model compared to the Helmholtz model (Fig. 9c). It is notable how the misfit evolution over the y-axis is dominated by the slope of the density heterogeneity in the true structure (red dashed line). The Helmholtz misfit values approach the full acoustic misfit values at a density gradient close to zero [see green highlight at y-receiver 6 in Fig. 9(c)], whereas, for steep changes in density at y-receiver 13 in the model, the Helmholtz equation performs relatively poorly.

Fig. 10 illustrates the effect of density gradients on phase velocity estimates at two specific receiver stations in the array. Phase velocity squared is given by the slope of the linear relationship between spatial and temporal gradients [eq. (24) for Helmholtz

and eq. (25) for full acoustic equation]. Fig. 10(a) shows that the full acoustic spatial gradients reveal a clearer linear relationship than the Helmholtz model as indicated by a coefficient of determination R^2 closer to 1. The difference in best fit slope estimates shows that phase velocity is considerably underestimated for the Helmholtz model at receiver [13,13] due to the fact that the relative density structure is neglected in the computation of the spatial gradients. This disparity in the accuracy of phase velocity estimates becomes evident also in the comparison of left-hand and right-hand side signals of the full acoustic and Helmholtz equation (Fig. 10b) and their respective residuals (Fig. 10c). They illustrate that the full acoustic expression matches the pure data vector well, whereas the Helmholtz expression exhibits larger residuals than the full acoustic case for both receiver stations. Incorporating density in the spatial gradient terms of WEI is thus shown to be important in order to estimate phase velocities accurately.

If we compare the misfit residuals for receiver [13,13] (Fig. 10c, left-hand panel) and [13,6] (Fig. 10c, right-hand panel), we can see
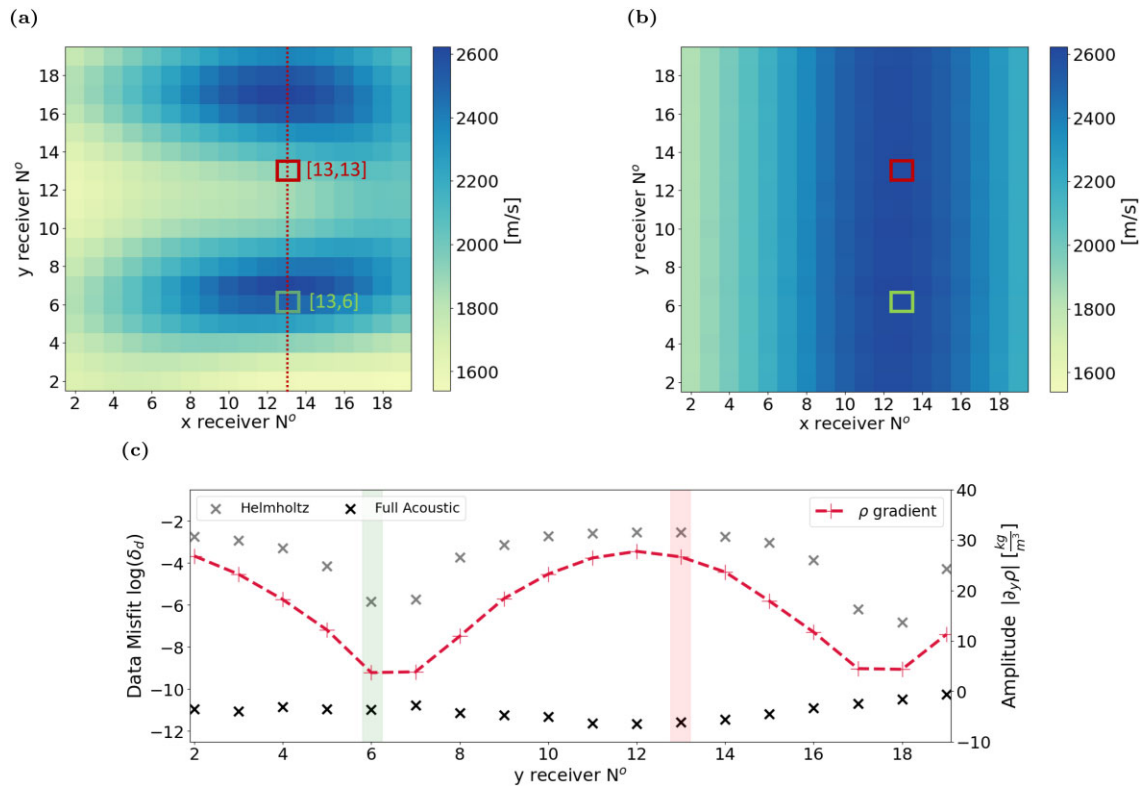
Figure 9. Phase velocity map estimated using (a) linear regression based on Helmholtz wave equation and (b) full acoustic wave equation inversion. Red and green squares mark receiver stations of interest [13,13] and [13,6]. (c) Data misfit post inversion averaged over all *x*-cross sections (red dotted line in (a) given at example of fixed receiver position $x = 13$) for both phase velocity maps (a) and (b). Black and grey crosses show the logarithm of misfit δ_d in eq. (52) for the Helmholtz equation (grey) and the full acoustic wave equation (black). The red dashed curve shows the absolute value of the *y*-gradient of the true density heterogeneity $\Delta\rho$. Green and red highlighting at receiver station 6 and 13 represent the respective positions in the 2-D plan view map.

that the full acoustic residuals are of the same order of magnitude at both stations whereas the Helmholtz residuals are two orders of magnitude larger for receiver [13,13]. Receiver [13,13] is located in an area where density is highly variable between the surrounding stations (26 kg m^{-3} from Fig. 9c) which explains why the Helmholtz wave equation is subject to much larger residuals than the full acoustic equation. Receiver [13,6] is in an area with only weak variations in density among neighbouring receivers (4 kg m^{-3} from Fig. 9c), so the left-hand sides of both Helmholtz and full acoustic equations agree well with the observed data vector. The accuracy of velocity estimates thus depends on the true density gradient across surrounding receivers when using the Helmholtz equation for WEI.

Changing data frequencies

The effect of the density gradient on phase velocity is persistent over a wider frequency range than was analysed above. In Figs 11(a) and (b), the dashed blue lines depict the true *P*-wave velocity in *y*- and *x*-direction, respectively, for the shallow layer 1 and the deeper layer 2 of the synthetic model (Fig. 3). Due to wave dispersion, the estimated phase velocities should lie in between those two expected absolute thresholds depending on the analysed frequency. The Helmholtz estimates for phase velocity (Fig. 11a) are consistently underestimated for receivers where density gradients are high (see Fig. 12 as reference), due to the use in WEI of discretization

coefficients that neglect the influence of density (Table 1), whereas they approximate full acoustic (Fig. 11b) phase velocity estimates at low density gradient values. However, the influence of the density gradients on the Helmholtz phase velocity estimates seems to become smaller with increasing frequency.

Accuracy of density gradient estimates seems to decrease with increasing frequency (Fig. 12): at a frequency of 6 Hz, the true gradient model in layer 1 is well approximated, whereas the result at frequency 14 Hz shows a clear discrepancy between true and estimated density gradients. A trend between errors on density gradients and strength of the density fingerprint (Fig. 12, right-hand panel) becomes notable: parameter errors on estimated density gradients via WEI increase with decreasing strength of the density signal. This suggests that higher frequencies are less sensitive to density.

For the model tested, no frequency dependence of the relative density gradient estimate is observed. This is likely due to the fact that the lower layer of the investigated model is homogeneous and consequently does not have an associated density fingerprint. From Fig. 7 we know that the bulk density estimate is influenced by the damping parameter of the inversion process. Testing the frequency dependence on the absolute density is possible if we hold the initial reference model in the inversion process constant over the narrow band-passed frequency bands. Fig. C1 in Appendix C shows that there is no clear increase of the absolute density estimate with decreasing frequency and thus the higher bulk density
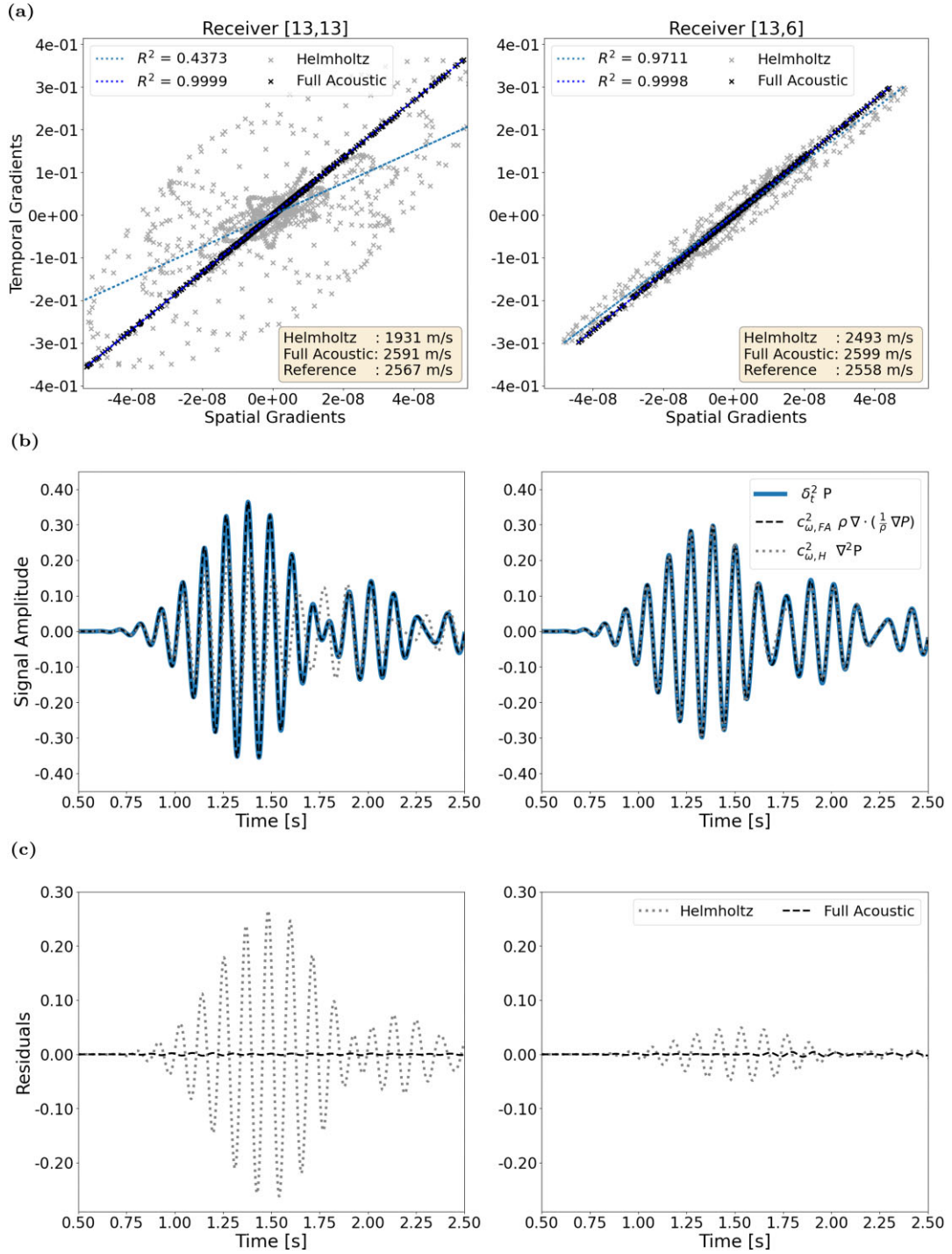
Figure 10. (a) Linear relationship between temporal gradients $\delta_t^2 P$ and $\rho \nabla \cdot \left(\frac{1}{\rho} \nabla P \right)$ from (49) for the full acoustic wave equation and $\nabla^2 P$ from eq. (48) for the Helmholtz wave equation at the two receiver locations shown in Fig. 9(a). The coefficient of determination R^2 denotes the goodness of fit of the data by the linear regression model, and phase velocity estimates using each equation are shown along with the reference velocity obtained for a homogeneous density forward model. (b) Discrete time-series of the observed data vector ($d = \delta_t^2 P$, solid blue) and the left-hand sides of both Helmholtz ($c_{\omega,H}^2 \nabla^2 P$, black dotted) and full acoustic ($c_{\omega,FA}^2 \rho \nabla \cdot \left(\frac{1}{\rho} \nabla P \right)$, grey dashed) wave equations, respectively, when using the estimated parameter values for phase velocity and density. (c) Respective residuals (difference between right-hand and left-hand side) of both Helmholtz and full acoustic wave equations.
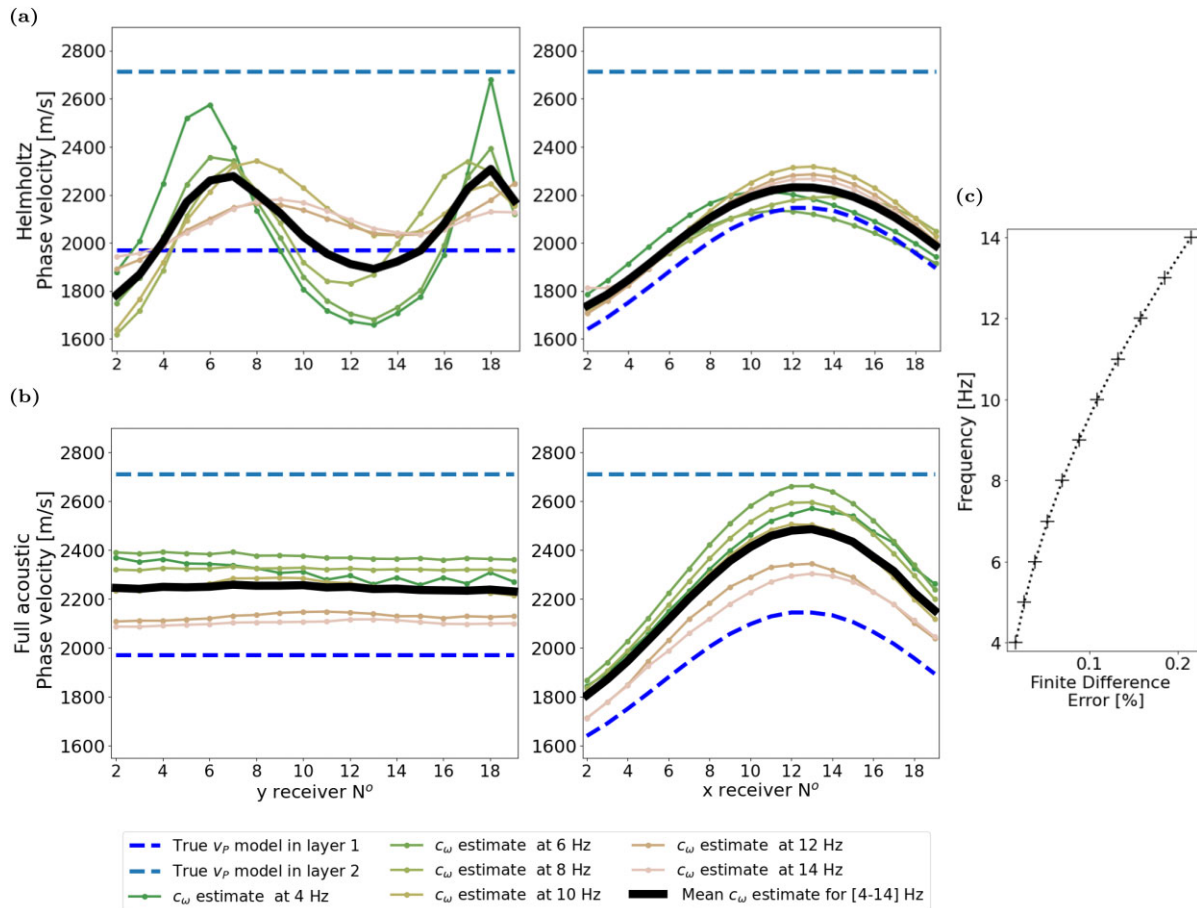
Figure 11. Results for the estimated phase velocities for 2 Hz wide bandpasses around central frequencies 4, 6, 8, 10, 12 and 14 Hz from Helmholtz linear regression (a) and full acoustic WEI (b). Estimated phase velocities are shown as a mean over all *x* (left-hand panel) and *y* (middle panel) cross-sections, respectively. For the estimation of full acoustic phase velocities, density information as shown in Fig. 12 is used. The mean value over all the frequency results is shown for both full acoustic and Helmholtz velocities in a black solid line. (c) shows the error evolution over frequency for the 2nd order accurate approximation of the spatial gradients with a spacing of 4 m used in this example (see Appendix A).

of the homogeneous lower layer does not seem to influence the estimates.

Fig. 13(d) shows how phase velocity perturbation increases with decreasing frequency and is roughly correlated with the signal strength of density. Full acoustic WEI can account for these density induced effects in phase velocity over a broad range of central filter frequencies, producing more accurate dispersion curves (Figs 13a–c). The full acoustic estimates display higher coefficients of determination (Fig. 13b) and lower misfits (Fig. 13c) than the Helmholtz results over all frequencies. As a reference we estimate a dispersion curve for the velocity model in Fig. 3 with a constant density of 1600 kg m^{-3} in layer 1 (Appendix B, Fig. B1) and compare it to dispersion curves obtained with full acoustic and Helmholtz WEI (Fig. 13a) for the variable density model (Fig. 3). The dispersion curve calculated on the basis of full acoustic WEI is able to reproduce the general trend of the reference dispersion curve. We do not expect a perfect match as the imposed density structure in the laterally heterogeneous case does influence the paths taken by wave energy. The Helmholtz dispersion curve does not reproduce the key feature of a classical dispersion curve where phase velocity increases with decreasing frequency. This shows that it is detrimental for depth model reconstruction to assume a constant density over

space in a medium with laterally heterogeneous density, especially at lower frequencies.

Random noise

Given that in real use case scenarios WEI depends on field recordings, it is important to consider the robustness of density estimation to errors in the recorded signal. The density signal is relatively weak compared to that of phase velocity, hence it may be obscured by instrumentation noise in the field. We add random noise, expressed as a percentage of the mean trace amplitude over the whole grid, to the simulated observed signals in order to determine a threshold of noise beneath which the method still delivers meaningful results. For each receiver, the added noise follows an uncorrelated normal distribution with a spread of 0.1–5 per cent of the mean trace amplitude.

Correlation factors for density decrease with increasing noise levels. At noise levels 0.1–1 per cent of the mean trace amplitude, the pressure with added noise remains relatively similar to the true pressure (Fig. 14a). The density distributions are thus centred around the optimal correlation line where true and estimated density match perfectly (Fig. 14b). At a random noise level of 5 per cent the
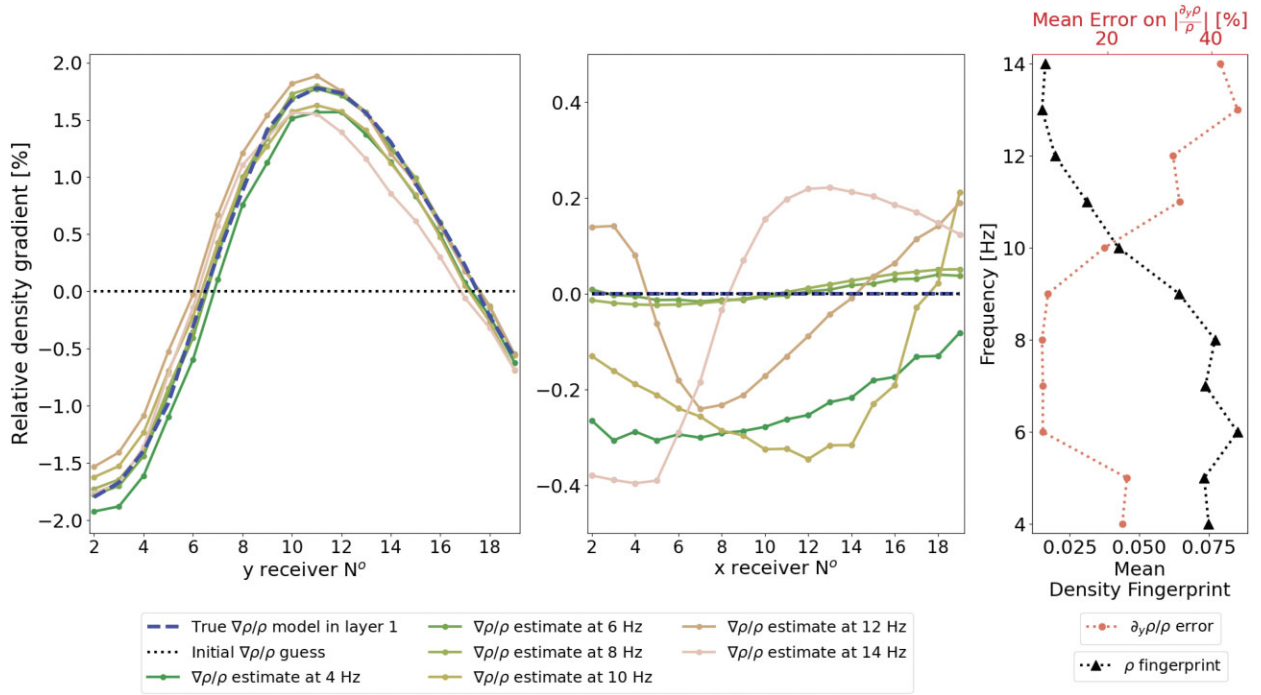
Figure 12. Results for density inversion at the lowest misfit iteration for 2 Hz wide bandpasses around central frequencies 4, 6, 8, 10, 12 and 14 Hz. Estimated density is shown as a mean over all x (left-hand panel) and y (middle panel) cross-sections, respectively. The right-hand panel shows the mean error (eq. 53) on relative y-gradients of density averaged over the whole array per analysed frequency. The mean density fingerprint for normalized spatial pressure gradients (eq. 50) is calculated for each frequency as $1/n_t \sum_{n=1}^{n_t} |\Gamma_n|$ and then averaged over the array.
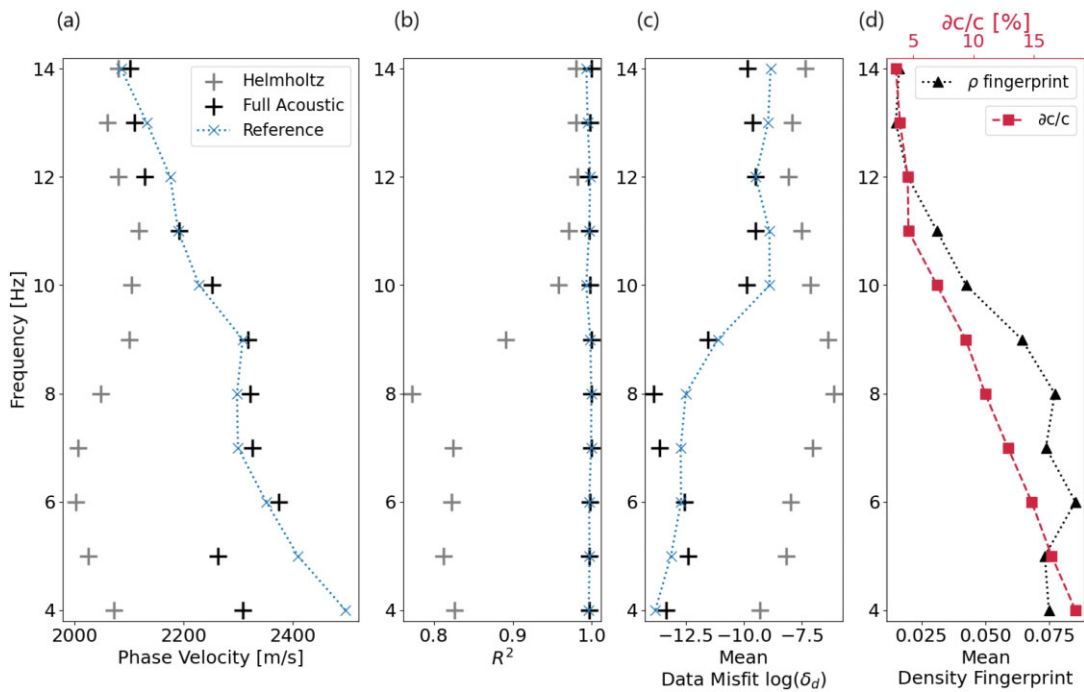
Figure 13. Mean phase velocity dispersion curve (a) over the whole array obtained via full acoustic WEI (black crosses) and Helmholtz WEI (grey crosses), respectively. Phase velocity results are obtained for a reference model (blue dotted line with cross marker) produced by the same setup as described in Fig. 3 but with constant density in layer 1 (Appendix B, Fig. B1). Corresponding coefficients of determination (b) and misfits (c) are shown to evaluate the data fit. (d) The perturbation of phase velocity $\frac{\partial c}{c}$ (red dashed line with square markers) is defined by the difference between phase velocity in the heterogeneous (grey crosses) and homogeneous baseline model (blue crosses) obtained via linear regression on the basis of the Helmholtz wave equation. The mean fingerprint Γ of the density signal is defined as in Fig. 12 and shown by black triangles.
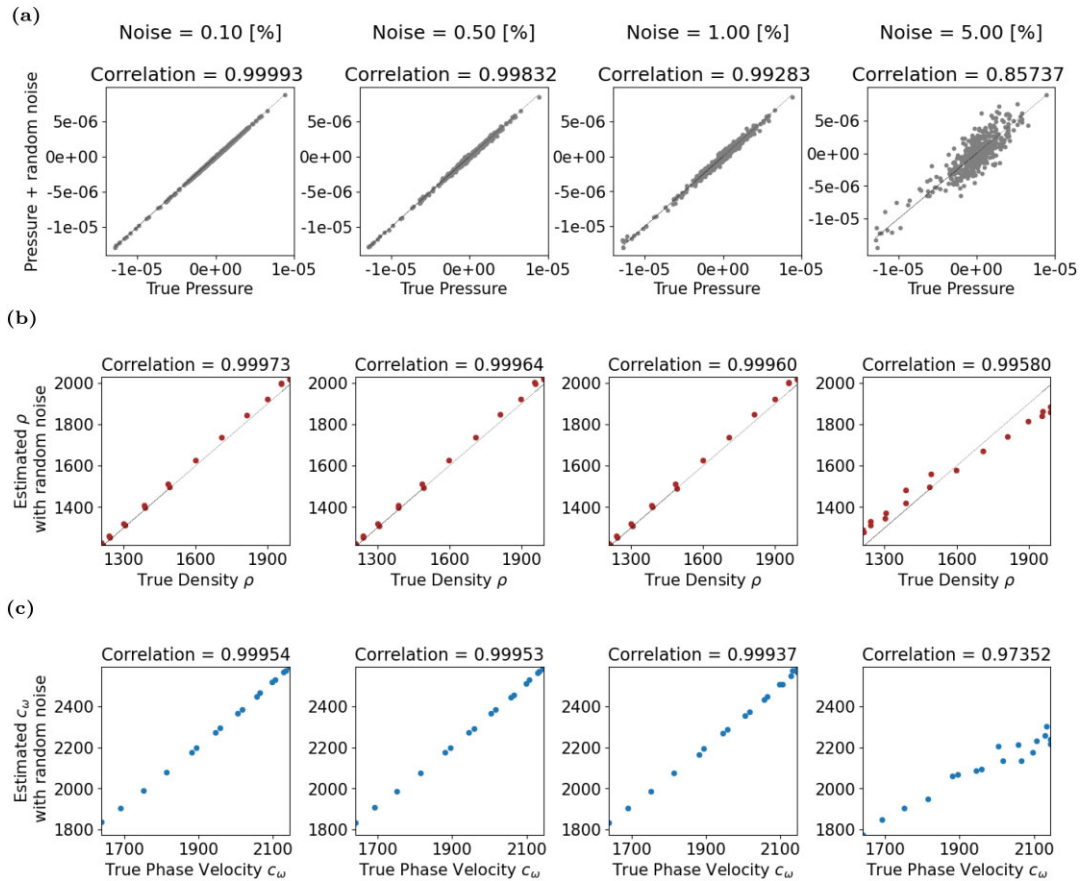
Figure 14. (a) Correlation plots between true pressure signal and pressure signal at 8 Hz with added random noise at 0.1, 0.5, 1 and 5 per cent of the mean amplitude of the modelled pressure signal over the whole grid. The black dotted line represents optimal correlation (correlation coefficient of 1). Wavefield arrivals at $t > 2$ s are used to visualize the effect of the added random noise on lower amplitude signals. Correlation plots of model material parameters at the various noise levels; the correlations between true and estimated (b) density and (c) phase velocity are shown. True phase velocity is taken at 0.9 of the *S*-wave speed in the surface layer, hence the frequency dependence is not taken into account as it is difficult to determine the expected phase velocity in a laterally heterogeneous medium.

density distribution does not approximate the optimal correlation line well which suggests that the relative density structure cannot be estimated accurately. The correlation of phase velocity is dominated by the quality of the density information and vice versa: correlation coefficient values follow the same deteriorating trend when the noise level becomes higher (Fig. 14c). The estimates for both phase velocity and density remain stable up to a noise level of 1 per cent, but even at a noise level of 5 per cent the main structural trends are still recognized.

6.1.2 Elastic data

The iterative full acoustic inversion procedure is now performed using data generated in an elastic medium for the calculated wavefield potential Φ (from eq. 7) for a central frequency of 8 Hz. The damping applied had to be 10 times stronger than in the acoustic case, with the damping factor at the initial stabilizing iteration equal to the mean amplitude of all recorded pressure signals. All subsequent iterations are carried out with 10 per cent of the initial damping. The results obtained for density (Fig. 15a) and relative density gradients (Fig. 15b) suggest that the structural trends of the true model in the *y*-direction can be estimated approximately, but contain substantially more artefacts than in the acoustic case (Fig. 6). The sinusoidal trend of the lateral heterogeneity in *y*-direction is recognizable but

its shape is not correct. These distortions are naturally also mapped into estimates of relative spatial density variations. The poorly constrained results in the *x*-direction demonstrate relative density gradients deviating from zero, especially between receiver 3–6 which does not agree with the constant true model.

By examining the parameter error in *x*- and *y*-directions individually it becomes apparent that the parameter error in the *x*-direction monotonically increases with iterations, whereas the parameter error on the relative gradient in *y*-direction at first steadily decreases until iteration 60 after which it also follows an increasing trend. Consequently, artefacts are mapped into the density result during the inversion process. False structural density features are thus estimated by the inversion which suggests a strong cross-talk with other material parameters. A trade-off with velocity could cause the trend in velocity gradients in the *x*-direction, thereby distorting density. By mapping a false trend originating from the velocity error into the *x*-direction density gradient, gradients in *y*-direction might compensate by over or underestimating the density variation. The inversion being strongly influenced by the velocity response suggests that density has less weight in the elastic medium compared to the acoustic case. This becomes apparent in the misfit function map that explores the phase velocity and density space, displaying trade-offs between parameters in the acoustic and elastic case (Fig. 16).
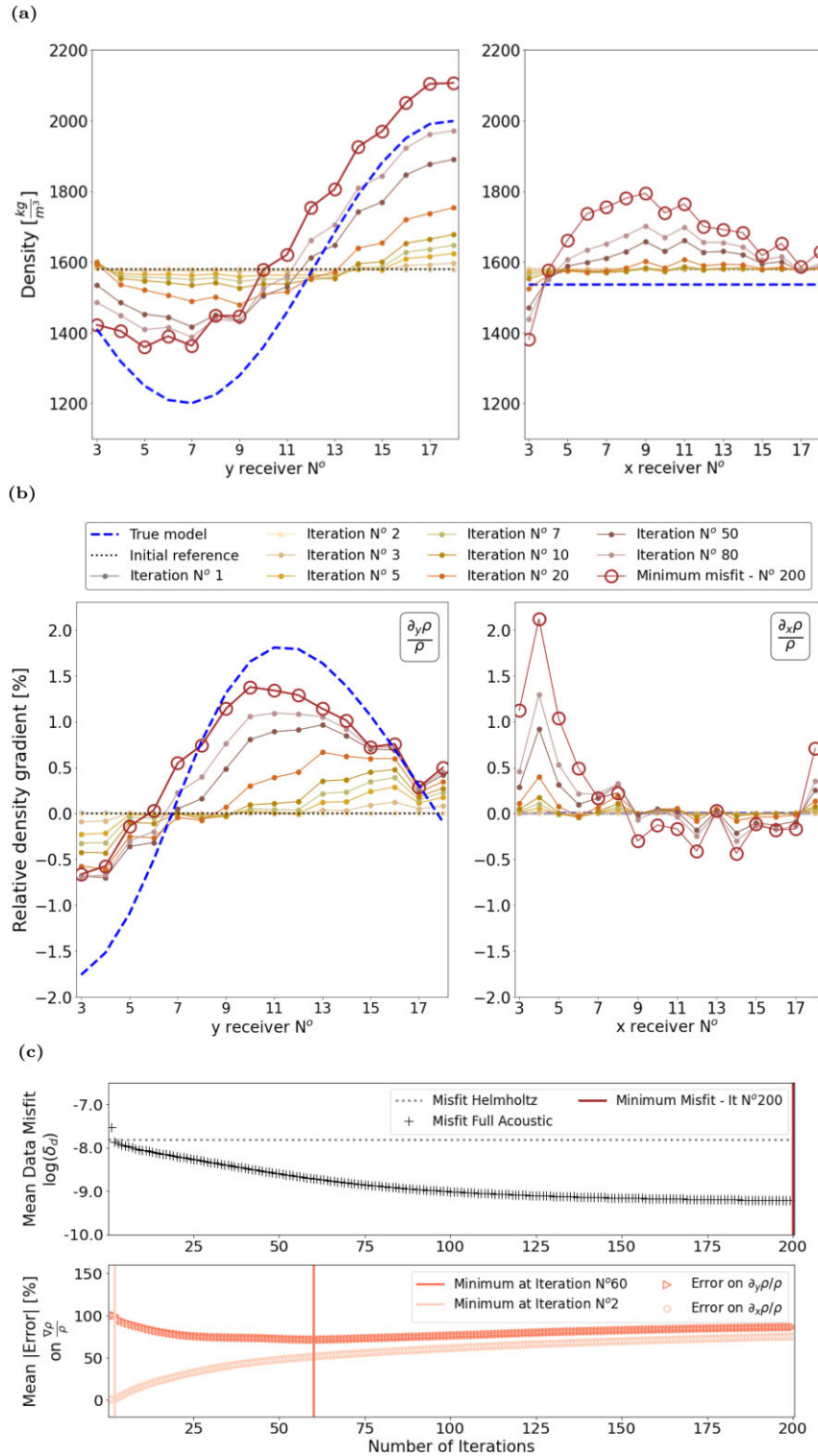
Figure 15. Inversion result for an elastic wavefield filtered to include a narrow frequency range around 8 Hz. Only the results for the internal receivers 3–18 are displayed, as boundary stations need to be disregarded for finite difference estimates and computing pressure entails an additional differentiation step in approximating the divergence of the displacement. Mean value of inverted (a) density and (b) relative density gradient results over all cross-sections in *x*-plane (left-hand panel) and *y*-plane (right-hand panel) showing the evolution of the inversion at selected stages during 200 iterations for a density model with sinusoidal heterogeneity as shown in Fig. 3. True model is depicted as dashed dark blue line and initial model as dotted black line. The minimum misfit result coincides with the last iteration 200 and is highlighted by red circles. (c) Logarithm of the mean data misfit over all internal receivers (upper row) for the full acoustic wave equation (black crosses) over 200 iterations. As a reference, the misfit achieved with linear regression based on the Helmholtz equation is shown by the dotted grey line. Mean parameter error on *x*- and *y*-relative gradients is shown in the lower row over all internal receivers. The respective minimum value positions are marked by vertical lines in red for minimum misfit at iteration 200, dark orange and light orange at iteration 60 and 2 for minimum parameter error on relative density gradients in *y*-direction and *x*-direction. The minimum mean gradiemeter error is evaluated after the initial stabilizing iteration.

(a) Acoustic
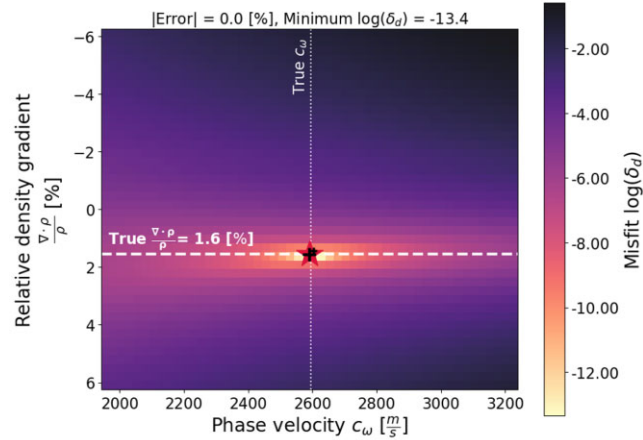
(b) Elastic
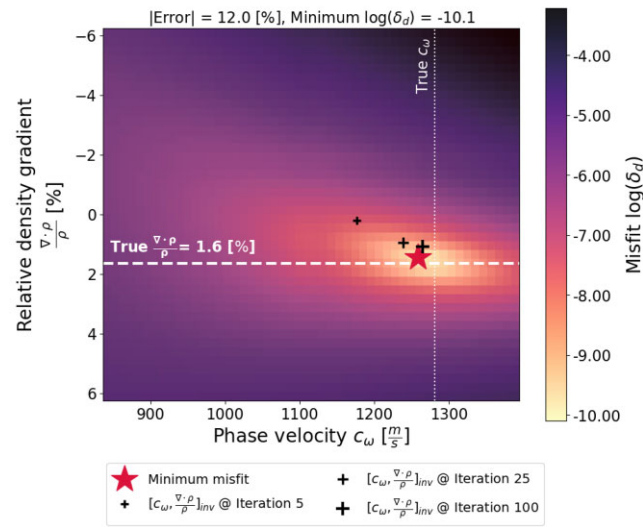
Figure 16. Misfit functions for (a) acoustic and (b) elastic media at receiver location [13,13] for a central frequency of 8 Hz. The misfit function are representative of the data used to produce Figs 6 and 15, respectively. The |Error| (eq. 53) shows the deviation of the relative density gradient value at the global minimum misfit in the grid search (red star) from the true value (white dashed line). Misfit is calculated as defined in eq. (52) and displayed for a single receiver. Crosses of increasing size show how total relative density gradient results of the iterative inversion process converges towards the global misfit of the grid search (small: iteration 5, medium: iteration 25, large: iteration 100). The true phase velocity c_ω (thin white dotted line) denotes the phase velocity obtained from full acoustic WEI when the true density structure is known.

6.1.3 Comparison between acoustic and elastic sensitivities

To visualize the sensitivities of the inversion towards the investigated parameters, we perform a grid search where we analyse a grid of potential solutions for phase velocity and relative density gradients, and their misfit to the true model (eq. 52) at a fixed central receiver location $[x_0, y_0]$ (Fig. 16). The density at the central location is fixed at the true value, but both neighbouring cells in the y-direction are freely variable in order to investigate the misfit evolution for various relative density gradient values. The density at $[y_0 + 1]$ and $[y_0 - 1]$ vary by ± 25 per cent around the true density value at $[x_0, y_0]$ and produce relative gradient values between

± 6.25 per cent. The phase velocity at the central point is variable around the phase velocity at $[x_0, y_0]$ obtained by full acoustic WEI and spans a range of ± 25 per cent.

We compare the misfit function for acoustic and elastic wavefield data at the central frequency of 8 Hz. At the example receiver [13,13], the global misfit minimum is about 3 orders of magnitudes lower in the acoustic case than in the elastic one. This suggests that more uncertainty is attached to the inversion process in the elastic medium given that wavefield traces have been normalized prior to the evaluation.

The misfit function distribution in the acoustic medium shows that density gradients are better constrained than phase velocities (Fig. 16a): for logarithm misfit values within two orders of magnitude from the minimum misfit [yellow area, $\log(\delta_d) < -11.4$], the phase velocity can vary up to 4 per cent whereas the relative density gradient is better constrained with no fluctuation at all over the applied binning. The absolute minimum misfit coincides exactly with the true value of the relative density gradient (|Error| = 0 per cent) and the minimum misfit phase velocity agrees well with the value of 2592 m s^{-1} obtained via full acoustic WEI using the true density structure. All iterations from the inversion process plot very closely to the global misfit due to the strong constraints on both parameters.

In elastic media, Fig. 16(b) shows that a comparatively larger number of relative density gradient and phase velocity values can explain the data on the basis of the full acoustic equation. For all solution pairs with misfit values within two orders of magnitude from the minimum misfit [yellow to orange area on Fig. 16(b), $\log(\delta_d) < -8.1$], density gradients vary between 12.8 per cent over the density gradient parameter space, whereas phase velocity fluctuates between 40.8 per cent over the phase velocity parameter space. The comparatively higher uncertainty than in the acoustic case might be attributed to the weaker density signal strength (Fig. 4) and approximations in physics. An error of 12 per cent between the true relative gradient and the value at the global minimum misfit suggests that the elastic data can not be fully explained by an underlying full acoustic wave equation. This implies that the inversion is prone to converge towards a slightly incorrect relative density gradient value. Iteration 5 of the inversion process gives an estimate on relative density gradient with a misfit value that is far away from the global misfit minimum (about two orders of magnitude) and provides a poor estimate on phase velocity and relative density gradient. Due to the comparatively poor constraints on both parameters, subsequent iterations are subject to parameter cross-talk and artefacts are mapped into the solution, corrupting primarily the relative gradient in the x-direction. Nevertheless, the inversion manages to converge towards a value in the vicinity of the true relative density gradient. To test the gradiometric estimate on phase velocity at the investigated receiver location, we use the surf-96 code (Herrman 2013) to calculate an expected value for mean Rayleigh wave velocity between 7 and 9 Hz from the generated dispersion curve. The phase velocity value of 1260 m s^{-1} corresponding to the lowest misfit marked by the red star in Fig. 16(b) is only 6 per cent smaller than the expected value of 1340 m s^{-1} generated by a 2 layer model matching the 1-D depth structure at the receiver location in our true model.

In summary, both acoustic and elastic media show sensitivity to relative density gradients. However, relative density gradients might not cause a large enough perturbation in the elastic wavefield to be sufficiently constrained in the inverse problem, whereas in acoustic media they are indeed essential to explain the data.

On seismic gradiometric wave equation inversion for density

6.2 Volumetric arrays

6.2.1 Elastic data

In a first step using a volumetric array, body wave velocities are estimated for a wavefield filtered between 7 and 9 Hz using a least-squares inversion from eq. (18). Those velocity results (Fig. 17a) are substituted into eqs (44) and (45) along with the calculated pressure. Pressure at the free surface is given in eq. (11), but we find that using only the related acoustic expression $P = K_a \nabla_H \cdot \boldsymbol{u}_H$ delivers more reasonable inversion results for density. Fig. 17 shows the estimated density results obtained by linear regression of eq. (46). The accuracy of the density results depends on how well the velocities can be estimated. The mean value of the relative parameter error over the receiver grid (Fig. 17b, right-hand panel) measures 3.04 per cent illustrating that the estimated results are close to the true parameter values. Once body wave velocities and densities are estimated, we can proceed to calculate Lamé parameters via empirical relationships: results are shown for the first Lamé parameter in Fig. 17(c).

7 DISCUSSION

We have shown that in acoustic media, relative density gradients of only 1.6 per cent produce a substantial change in the synthetic wavefield. This allows us to set up an inverse problem that successfully estimates density structure of the medium. The WEI approach has been demonstrated both for models in which density and velocity structure are uncorrelated, as well as structurally more common models that approximate geological interfaces in which density and velocity are correlated. Relative density contrasts down to an amplitude of 0.5 per cent can be imaged with a parameter error smaller than 10 per cent (Fig. 7). First tests suggest that the inversion process is robust for random noise up to 1 per cent of the mean trace amplitude (Fig. 14) which encourages a future trial on real data.

In elastic media, other effects interfere with the density signal, making density estimation more difficult from surface array data alone. Elastic results (Section 6.1.2) and sensitivity analysis (Section 6.1.3) show that there is sensitivity to relative density gradients in elastic media. However, the full acoustic approximation is too severe for elastic wave physics and density is too weakly constrained to be fully estimated using the proposed iterative inversion process. This makes it unlikely that density inversion based on full acoustic WEI will be feasible in an elastic Earth, or worse a viscoelastic Earth where the already small density signal might be overshadowed by the addition of energy dissipation. The full acoustic method might only be applicable in localized areas where the wavefield passes predominantly through gas or liquids.

To estimate density in elastic media it is therefore necessary to use volumetric array measurements and to adopt a more accurate representation of underlying wave physics as a basis for gradiometric WEI, such as the full elastic wave equation. However, it became clear from eq. (3a) that if we only measure particle velocity or displacement and if the source term $\boldsymbol{f}$ is omitted, density does not appear as an independent term outside of the expressions for body wave velocity. It is therefore impossible to estimate density independently of the Lamé parameters using a sourceless full elastic equation. However, if both displacement and pressure are measured in a dual sensor configuration, the full elastic wave equation at the free surface exhibits a direct, independent sensitivity to density in the form of a linear relationship between pressure and displacement terms (Section 6.2). If we are willing to deploy buried receivers

then the results herein suggest that density can be estimated directly from recorded data, together with *P*- and *S*-wave velocities. Pressure sensors for solid earth applications have been presented as a prototype (Edme *et al.* 2018), but reliable pressure measurements are not readily available as of now.

While our focus herein has been to make use of the ambient wavefield, an alternative exists if we consider the introduction of a local source within the receiver array. In that case, if the associated body force term $\boldsymbol{f}$ is clearly defined, density can be isolated within the wave equation (see eq. 56) and could in theory be estimated. We therefore propose a thought experiment in which we consider a weight drop within a 3-D gradiometric receiver array (Fig. 1a) and perform volumetric gradiometry. If we assume that the weight drop acts as a vertical point load on the surface then the body force $\boldsymbol{f}$ is generally defined as a distribution of force density as a function of position and time (Madariaga 2007):

$$\boldsymbol{f}(\boldsymbol{x}, t) = \boldsymbol{f_0}\, s(t)\, \delta(\boldsymbol{x} - \boldsymbol{x_0}), \tag{54}$$

where $\boldsymbol{f_0}$ is a unit vector in the direction of the point force $\boldsymbol{f_0} = [0, 0, 1]^T$, $s(t)$ is a source–time function (the variation of the amplitude of the force as a function of time) applied in the vertical direction and $\delta(\boldsymbol{x} - \boldsymbol{x_0})$ is the Dirac distribution centred at the source location $\boldsymbol{x_0}$. Neitzel (1958) first analysed the seismic characteristics of a weight-drop source in a field experiment: he measured the force applied to the ground in an effort to characterize the source term and recorded the wavefield response. Several authors thereafter proposed source term expressions to explain wavefield observations produced by a weight drop: based on the work of Lamb (1904), Pekeris (1955) and Mooney (1974) derived analytical expressions of the wavefield response at the free surface due to the application of an arbitrary excitation. The use of Heaviside step function and Dirac Delta function could not reproduce wavefield quantities accurately, whereas a sinusoidal source–time function was shown to better approximate the resulting wavefield (Abe *et al.* 1990). Defining a generalized source term as accurately as possible is an essential task in predicting the Earth response to a weight drop, and hence also in the proposed application to gradiometry. Colombero *et al.* (2015) found that the source–time function in the near-field of a weight drop can be represented by a modified Gabor wavelet [based on Semblat & Pecker (2009)] expressed in terms of particle velocity:

$$s(t) = \begin{cases} C_b\, \beta\, t^\gamma\, exp\left[-\left(\frac{2\pi}{T_s\, \alpha} t\right)^2\right] cos\left(\frac{2\pi}{T_s} t\right) & \text{if } 0 \leq t \leq 1.2 T_s \\ 0 & \text{otherwise,} \end{cases} \tag{55}$$

where t is a generic time instant, T_s the period of the function, C_b the momentum of the dropped weight and α, β and γ are constants whose corresponding values are given in Colombero *et al.* (2015). By comparing recorded particle velocity from drop load tests and synthetic data generated by propagating the proposed source signal, they found that simulated and real impulse responses in the near-field of the source match well.

We therefore propose that in the case where we allow ourselves the luxury of a local source, the modified Gabor source–time wavelet (eq. 55) could in principle be incorporated in the volumetric gradiometry workflow in order to estimate density on the basis of the full elastic wave equation at the free surface. Alternatively, one could use a piezoelectric sensor as a controlled source using a preset electrical current signal (e.g. a Ricker wavelet) to drive the resulting vibrations at the source point in the form of a known source–time function. In a first step we consider eq. (3a) without body forces.
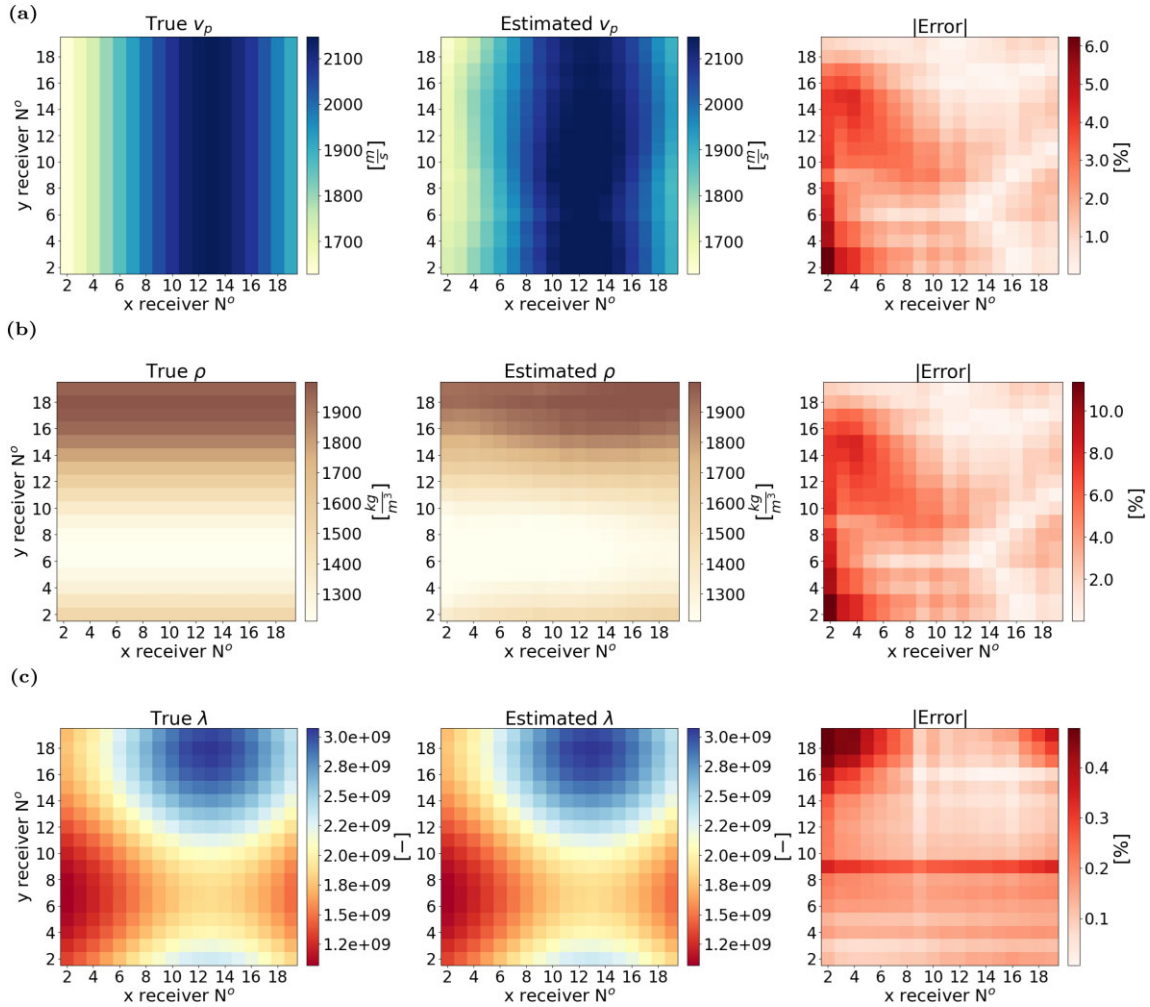
Figure 17. Plan view of (left-hand column) true model and (middle column) gradiometric estimates of material parameters. The corresponding parameter error (eq. 53) is shown in the right-hand column. Rows (a), (b) and (c) correspond to results for *P*-wave velocity, density and the first Lamé parameter λ. Velocities are estimated via WEI of eq. (18), densities by linear regression of eq. (46) and Lamé parameters are obtained from the latter estimated velocity and density results where $\lambda = (v_P^2 - 2v_S^2)\rho$.

We can then estimate *P*-wave velocity $v_{P,e}$ and *S*-wave velocity $v_{S,e}$ at the free surface for any incoming wavefield using volumetric gradiometric measurements and the Lax–Wendroff correction (Lax & Wendroff 1964) as proposed by Curtis & Robertsson (2002). Then by applying body forces in the form of a weight drop where $s(t)$ is clearly defined (eq. 55), eq. (18) that describes the vertical component of a wavefield $\boldsymbol{\theta} = [\theta_x, \theta_y, \theta_z]$ at the free surface takes the form:

$$\left[\partial_t^2 \, \theta_z - v_{P,e}^2 \, A_z(t) \, + \, v_{S,e}^2 \, B_z(t) \right] \rho \; = f_z \tag{56}$$

with $A_z(t)$ and $B_z(t)$ given in eqs (19) to (20). The entire left-hand side of equation (56) is then known apart from density, so this equation sets up a linear inverse problem which might be solved for density.

8 CONCLUSION

We investigated whether surface wavefield gradiometry can be used to gain insights into material density via WEI of the full acoustic wave equation in both 3-D acoustic as well as 3-D elastic media using ambient noise data. We propose and test an iterative inversion scheme for both density and phase velocity based on gradiometric WEI and surface recordings of simulated ambient noise. No inherent scaling between velocity and density is imposed, making it suitable to detect density changes caused by temperature or chemically induced mechanisms. Synthetic results for 3-D acoustic media suggest that it is possible to estimate relative density structure with WEI by using a full acoustic formulation for wave propagation along the surface. We show that using a constant density assumption for the medium can be detrimental to subsurface velocity images, whereas the full acoustic formulation of gradiometry improves our knowledge of all material properties. It allows us to estimate density as an additional material parameter as well as to improve phase velocity estimates by incorporating approximations of the density structure.

By expanding this methodology to the elastic case, we tested the feasibility of estimating density in the solid Earth with gradiometric WEI on the basis of a full acoustic approximation. The dilatational component of Rayleigh waves at the free surface was shown to be imprinted by effects from relative density changes in the medium. It proved however to be more difficult to obtain reliable estimates on relative density changes in elastic media than in acoustic media due to a stronger trade-off between density and phase velocity caused

by the difference in the measured wave type sensitivities to material parameters in both analysed media. However, using a 3-D array and the full elastic wave equation at the free surface it is possible to obtain reliable absolute density estimates in elastic media. We suggest that another reasonable way to obtain density estimates in elastic media would be to fire a local source and include the corresponding source term within an inversion of the full elastic wave equation.

DATA AVAILABILITY

All code used in this study is publicly available at https://github.com/mafab1994/density_WEI. The synthetic data were produced using the Salvus software package from Mondaic AG and are made available as a repository on Kaggle at https://www.kaggle.com/dsv/7593971.

REFERENCES

Abe, S., Kobayashi, Y. & Ikawa, T., 1990. Seismic characteristics of the weight-dropping source, *J. Phys. Earth,* **38**(3), 189–212.

Afanasiev, M., Boehm, C., van Driel, M., Krischer, L., Rietmann, M., May, D.A., Knepley, M.G. & Fichtner, A., 2019. Modular and flexible spectral-element waveform modelling in two and three dimensions, *Geophys. J. Int.,* **216**(3), 1675–1692.

Aki, K. & Richards, P.G., 2002. *Quantitative Seismology,* 2nd edn, University Science Book.

Amundsen, L., Røsten, T., Robertsson, J.O. & Kragh, E., 2005. Rough-sea deghosting of streamer seismic data using pressure gradient approximations, *Geophysics,* **70**(1), V1–V9.

Anderson, S.P., von Blanckenburg, F. & White, A.F., 2007. Physical and chemical controls on the critical zone, *Elements,* **3**(5), 315–319.

Befus, K., Sheehan, A., Leopold, M., Anderson, S. & Anderson, R., 2011. Seismic constraints on critical zone architecture, boulder creek watershed, *Vadose Zone J.,* **10**(3), 915–927.

Bergmann, P.G., 1946. The wave equation in a medium with a variable index of refraction, *J. acoust. Soc. Am.,* **17**(4), 329–333.

Blanch, J. & Robertsson, J.O., 1997. A modified Lax-Wendroff correction for wave propagation in media described by Zener elements, *Geophys. J. Int.,* **131**(2), 381–386.

Blom, N., Boehm, C. & Fichtner, A., 2017. Synthetic inversions for density using seismic and gravity data, *Geophys. J. Int.,* **209**(2), 1204–1220.

Blom, N., Gokhberg, A. & Fichtner, A., 2020. Seismic waveform tomography of the central and eastern Mediterranean upper mantle, *Solid Earth,* **11**(2), 669–690.

Boddice, D., Metje, N. & Tuckwell, G., 2019. Quantifying the effects of near surface density variation on quantum technology gravity and gravity gradient instruments, *J. appl. Geophys.,* **164,** 160–178.

Boddice, D., Metje, N. & Tuckwell, G., 2022. Microgravity surveying before, during and after distant large earthquakes, *J. appl. Geophys.,* **197,** doi:10.1016/j.jappgeo.2022.104542.

Brimhall, G.H. *et al.*, 1992. Deformational mass transport and invasive processes in soil evolution, *Science,* **255**(5045), 695–702.

Cance, P. & Capdeville, Y., 2015. Validity of the acoustic approximation for elastic waves in heterogeneous media acoustic approximation of elastic waves, *Geophysics,* **80**(4), T161–T173.

Cao, R., Earp, S., de Ridder, S.A., Curtis, A. & Galetti, E., 2020. Near-real-time near-surface 3d seismic velocity and uncertainty models by wavefield gradiometry and neural network inversion of ambient seismic noise, *Geophysics,* **85**(1), KS13–KS27.

Choi, Y., Min, D.-J. & Shin, C., 2008. Frequency-domain elastic full waveform inversion using the new pseudo-hessian matrix: experience of elastic Marmousi-2 synthetic data, *Bull. seism. Soc. Am.,* **98**(5), 2402–2415.

Colombero, R., Kontoe, S., Foti, S. & Potts, D., 2015. Numerical modelling of drop load tests, *Soil Dyn. Earthq. Eng.,* **77,** 279–289.

Curtis, A. & Robertsson, J.O., 2002. Volumetric wavefield recording and wave equation inversion for near-surface material properties, *Geophysics,* **67**(5), 1602–1611.

Curtis, A., Gerstoft, P., Sato, H., Snieder, R. & Wapenaar, K., 2006. Seismic interferometry—turning noise into signal, *Leading Edge,* **25**(9), 1082–1092.

De Ridder, S. & Biondi, B., 2015. Near-surface Scholte wave velocities at Ekofisk from short noise recordings by seismic noise gradiometry, *Geophys. Res. Lett.,* **42**(17), 7031–7038.

De Ridder, S. & Curtis, A., 2017. Seismic gradiometry using ambient seismic noise in an anisotropic earth, *Geophys. J. Int.,* **209**(2), 1168–1179.

Dexter, A., 2004. Soil physical quality: Part I. Theory, effects of soil texture, density, and organic matter, and effects on root growth, *Geoderma,* **120**(3–4), 201–214.

Edme, P. & Yuan, S., 2016. Local dispersion curve estimation from seismic ambient noise using spatial gradients, *Interpretation,* **4**(3), SJ17–SJ27.

Edme, P., Muyzert, E., Goujon, N., El Allouche, N. & Kragh, E., 2018. Seismic wavefield divergence at the free surface, *First Break,* **36**(12), 75–82.

Fanchi, J.R., 2010. 7 - well logging, in *Integrated Reservoir Asset Management,* pp. 109–124, ed. Fanchi, J.R., Gulf Professional Publishing.

Fichtner, A., 2010. *Full Seismic Waveform Modelling and Inversion,* Springer Science & Business Media.

Flinchum, B.A., Holbrook, W.S., Grana, D., Parsekian, A.D., Carr, B.J., Hayes, J.L. & Jiao, J., 2018. Estimating the water holding capacity of the critical zone using near-surface geophysics, *Hydrol. Process.,* **32**(22), 3308–3326.

Flinchum, B.A., Holbrook, W.S. & Carr, B.J., 2022. What do P-wave velocities tell us about the critical zone?, *Front. Water,* **3,** doi:10.3389/frwa.2021.772185.

Foti, S. *et al.*, 2018. Guidelines for the good practice of surface wave analysis: a product of the Interpacific project, *Bull. Earthq. Eng.,* **16,** 2367–2420.

Friederich, W., Hunzinger, S. & Wielandt, E., 2000. A note on the interpretation of seismic surface waves over three-dimensional structures, *Geophys. J. Int.,* **143**(2), 335–339.

Gardner, G., Gardner, L. & Gregory, A., 1974. Formation velocity and density—the diagnostic basics for stratigraphic traps, *Geophysics,* **39**(6), 770–780.

Gavete, L., Gavete, M. & Benito, J., 2003. Improvements of generalized finite difference method and comparison with other meshless method, *Appl. Math. Modell.,* **27**(10), 831–847.

Geiger, H.D. & Daley, P.F., 2003. Finite difference modelling of the full acoustic wave equation in Matlab. CREWES Research Report. https://api.semanticscholar.org/CorpusID:124434193.

Handoyo, H. *et al.*, 2022. Geophysical imaging of the critical zone along the Eastern Betic Shear Zone (EBSZ), SE Iberian Peninsula, *Appl. Sci.,* **12**(7), doi:10.3390/app12073398.

Herrman, R., 2013. Computer programs in seismology: an evolving tool for instruction and research, *Seismol. Res. Lett.,* **84**(6), 1081–1088.

Holbrook, W.S. *et al.*, 2014. Geophysical constraints on deep weathering and water storage potential in the Southern Sierra Critical Zone observatory, *Earth Surf. Process. Landform.,* **39**(3), 366–380.

Holbrook, W.S., Marcon, V., Bacon, A.R., Brantley, S.L., Carr, B.J., Flinchum, B.A., Richter, D.D. & Riebe, C.S., 2019. Links between physical and chemical weathering inferred from a 65-m-deep borehole through earth's critical zone, *Sci. Rep.,* **9**(1), doi:10.1038/s41598-019-40819-9.

Huang, C., Shao, M. & Tan, W., 2011. Soil shrinkage and hydrostructural characteristics of three swelling soils in Shaanxi, China, *J. Soils Sediment.,* **11,** 474–481.

Huiskamp, G., 1991. Difference formulas for the surface Laplacian on a triangulated surface, *J. Comput. Physics,* **95**(2), 477–496.

Ivanov, J., Tsoflias, G., Miller, R.D., Peterie, S., Morton, S. & Xia, J., 2016. Impact of density information on Rayleigh surface wave inversion results, *J. appl. Geophys.,* **135,** 43–54.

James, S., Knox, H., Abbott, R., Panning, M. & Screaton, E., 2019. Insights into permafrost and seasonal active-layer dynamics from ambient seismic noise monitoring, *J. geophys. Res.,* **124**(7), 1798–1816.

Jeong, W., Lee, H.-Y. & Min, D.-J., 2012. Full waveform inversion strategy for density in the frequency domain, *Geophys. J. Int.,* **188**(3), 1221–1242.

Karato, S.-i. & Karki, B.B., 2001. Origin of lateral variation of seismic wave velocities and density in the deep mantle, *J. geophys. Res.,* **106**(B10), 21771–21783.

Kaufman, A.A., Levshin, A.L. & Larner, K.L., 2000. *Acoustic and Elastic Wave Fields in Geophysics,* Vol. **2,** Gulf Professional Publishing.

Köhn, D., De Nil, D., Kurzmann, A., Przebindowska, A. & Bohlen, T., 2012. On the influence of model parametrization in elastic full waveform tomography, *Geophys. J. Int.,* **191**(1), 325–345.

Lamb, H., 1904. I. on the propagation of tremors over the surface of an elastic solid, *Phil. Trans. R. Soc. Lond., A,* **203**(359–371), 1–42.

Langston, C.A., 2007a. Spatial gradient analysis for linear seismic arrays, *Bull. seism. Soc. Am.,* **97**(1B), 265–280.

Langston, C.A., 2007b. Wave gradiometry in two dimensions, *Bull. seism. Soc. Am.,* **97**(2), 401–416.

Langston, C.A., 2007c. Wave gradiometry in the time domain, *Bull. seism. Soc. Am.,* **97**(3), 926–933.

Lax, P.D. & Wendroff, B., 1964. Difference schemes for hyperbolic equations with high order of accuracy, *Commun. Pure Appl. Math.,* **17**(3), 381–398.

Liang, C. & Langston, C.A., 2009. Wave gradiometry for USArray: Rayleigh waves, *J. geophys. Res.,* **114**(B2), doi:10.1029/2008JB005918.

Liang, C., Cao, F., Liu, Z. & Chang, Y., 2023. A review of the wave gradiometry method for seismic imaging, *Earthq. Sci.,* **36**(3), 254–281.

Lin, F.-C., Tsai, V.C. & Ritzwoller, M.H., 2012. The local amplification of surface waves: a new observable to constrain elastic velocities, density, and anelastic attenuation, *J. geophys. Res.,* **117**(B6), doi:10.1029/2012JB009208.

Liszka, T. & Orkisz, J., 1980. The finite difference method at arbitrary irregular grids and its application in applied mechanics, *Comput. Struct.,* **11**(1–2), 83–95.

Liu, Y. & Holt, W.E., 2015. Wave gradiometry and its link with Helmholtz equation solutions applied to USArray in the eastern us, *J. geophys. Res.,* **120**(8), 5717–5746.

Luo, J. & Wu, R.-S., 2018. Velocity and density reconstruction based on scattering angle separation, *Pure appl. Geophys.,* **175,** 4371–4387.

Madariaga, R., 2007. Seismic source theory, *Earthq. Seismol.,* **4,** 59–82.

Maeda, T., Nishida, K., Takagi, R. & Obara, K., 2016. Reconstruction of a 2D seismic wavefield by seismic gradiometry, *Prog. Earth planet. Sci.,* **3**(1), 1–17.

Miller, S.L. & Stewart, R.R., 1991. The relationship between elastic-wave velocities and density in sedimentary rocks: a proposal, CREWES Research Report, pp. 260–273.

Mooney, H.M., 1974. Some numerical solutions for lamb's problem, *Bull. seism. Soc. Am.,* **64**(2), 473–491.

Mosca, I., Cobden, L., Deuss, A., Ritsema, J. & Trampert, J., 2012. Seismic and mineralogical structures of the lower mantle from probabilistic tomography, *J. geophys. Res.,* **117**(B6), doi:10.1029/2011JB008851.

Muijs, R., Holliger, K. & Robertsson, J.O., 2002. Perturbation analysis of an explicit wavefield separation scheme for P- and S-waves, *Geophysics,* **67**(6), 1972–1982.

Muyzert, E. & Snieder, R., 2000. An alternative parameterisation for surface waves in a transverse isotropic medium, *Phys. Earth planet. Inter.,* **118**(1–2), 125–133.

Nabighian, M.N. et al., 2005. Historical development of the gravity method in exploration historical development of gravity method, *Geophysics,* **70**(6), 63ND–89ND.

Nakata, N., Gualtieri, L. & Fichtner, A., 2019. *Seismic Ambient Noise,* Cambridge Univ. Press.

Nanko, K. et al., 2014. A pedotransfer function for estimating bulk density of forest soil in japan affected by volcanic ash, *Geoderma,* **213,** 36–45.

Neitzel, E.B., 1958. Seismic reflection records obtained by dropping a weight, *Geophysics,* **23**(1), 58–80.

Nielson, T., Bradford, J., Holbrook, W.S. & Seyfried, M., 2021. The effect of aspect and elevation on critical zone architecture in the reynolds creek critical zone observatory: a seismic refraction study, *Front. Water,* **3,** doi:10.3389/frwa.2021.670524.

Nolet, G. et al., 1977. The upper mantle under western Europe inferred from the dispersion of Rayleigh modes, *J. Geophys.,* **43**(1), 265–285.

Oakley, D.O., Forsythe, B., Gu, X., Nyblade, A.A. & Brantley, S.L., 2021. Seismic ambient noise analyses reveal changing temperature and water signals to 10s of meters depth in the critical zone, *J. geophys. Res.,* **126**(2), e2020JF005823.

Obermann, A., Kraft, T., Larose, E. & Wiemer, S., 2015. Potential of ambient seismic noise techniques to monitor the St. Gallen geothermal site (Switzerland), *J. geophys. Res.,* **120**(6), 4301–4316.

Operto, S. & Miniussi, A., 2018. On the role of density and attenuation in three-dimensional multiparameter viscoacoustic VTI frequency-domain FWI: an OBC case study from the North Sea, *Geophys. J. Int.,* **213**(3), 2037–2059.

Pan, L., Chen, X., Wang, J., Yang, Z. & Zhang, D., 2019. Sensitivity analysis of dispersion curves of Rayleigh waves with fundamental and higher modes, *Geophys. J. Int.,* **216**(2), 1276–1303.

Pan, W., Geng, Y. & Innanen, K.A., 2018. Interparameter trade-off quantification and reduction in isotropic-elastic full-waveform inversion: synthetic experiments and hussar land data set application, *Geophys. J. Int.,* **213**(2), 1305–1333.

Parsekian, A., Singha, K., Minsley, B.J., Holbrook, W.S. & Slater, L., 2015. Multiscale geophysical imaging of the critical zone, *Rev. Geophys.,* **53**(1), 1–26.

Pekeris, C., 1955. The seismic surface pulse, *Proc. Natl. Acad. Sci.,* **41**(7), 469–480.

Piccolroaz, S., Majone, B., Palmieri, F., Cassiani, G. & Bellin, A., 2015. On the use of spatially distributed, time-lapse microgravity surveys to inform hydrological modeling, *Water Resour. Res.,* **51**(9), 7270–7288.

Płonka, A., Blom, N. & Fichtner, A., 2016. The imprint of crustal density heterogeneities on regional seismic wave propagation, *Solid Earth,* **7**(6), 1591–1608.

Prieux, V., Brossier, R., Operto, S. & Virieux, J., 2013. Multiparameter full waveform inversion of multicomponent ocean-bottom-cable data from the Valhall Field. Part 1: Imaging compressional wave speed, density and attenuation, *Geophys. J. Int.,* **194**(3), 1640–1664.

Qiao, J., Zhu, Y., Jia, X., Huang, L. & Shao, M., 2019. Development of pedotransfer functions for predicting the bulk density in the critical zone on the Loess Plateau, China, *J. Soils Sediment.,* **19,** 366–372.

Resovsky, J. & Trampert, J., 2003. Using probabilistic seismic tomography to test mantle velocity–density relationships, *Earth planet. Sci. Lett.,* **215**(1–2), 121–134.

Riebe, C.S., Hahm, W.J. & Brantley, S.L., 2017. Controls on deep critical zone architecture: a historical review and four testable hypotheses, *Earth Surf. Process. Landform.,* **42**(1), 128–156.

Robertsson, J.O. & Curtis, A., 2002. Wavefield separation using densely deployed three-component single-sensor groups in land surface-seismic recordings, *Geophysics,* **67**(5), 1624–1633.

Robertsson, J.O. & Kragh, E., 2002. Rough-sea deghosting using a single streamer and a pressure gradient approximation, *Geophysics,* **67**(6), 2005–2011.

Robertsson, J.O. & Muyzert, E., 1999. Wavefield separation using a volume distribution of three component recordings, *Geophys. Res. Lett.,* **26**(18), 2821–2824.

Robertsson, J.O., Levander, A., Symes, W.W. & Holliger, K., 1995. A comparative study of free-surface boundary conditions for finite-difference simulation of elastic/viscoelastic wave propagation, in *SEG Technical Program Expanded Abstracts 1995,* pp. 1277–1280, Society of Exploration Geophysicists.

Schmelzbach, C. *et al.*, 2018. Advances in 6C seismology: applications of combined translational and rotational motion measurements in global and exploration seismology advances in 6C seismology, *Geophysics,* **83**(3), WC53–WC69.

Semblat, J. & Pecker, A., 2009. *Waves and Vibrations in Soils: Earthquakes, Traffic, Shocks, Construction Works,* IUSS Press I.

Shaiban, A., De Ridder, S. & Curtis, A., 2022. Wavefield reconstruction and wave equation inversion for seismic surface waves, *Geophys. J. Int.,* **229**(3), 1870–1880.

Shapiro, N., Campillo, M., Margerin, L., Singh, S., Kostoglodov, V. & Pacheco, J., 2000. The energy partitioning and the diffusive character of the seismic coda, *Bull. seism. Soc. Am.,* **90**(3), 655–665.

Shearer, P.M., 2019. *Introduction to Seismology,* Cambridge Univ. Press.

Sollberger, D., Schmelzbach, C., Robertsson, J.O., Greenhalgh, S.A., Nakamura, Y. & Khan, A., 2016. The shallow elastic structure of the lunar crust: new insights from seismic wavefield gradient analysis, *Geophys. Res. Lett.,* **43**(19), 10–078.

Sollberger, D. *et al.*, 2020. Seismological processing of six degree-of-freedom ground-motion data, *Sensors,* **20**(23), doi:10.3390/s20236904.

Sollberger, D., Bradley, N., Edme, P. & Robertsson, J.O., 2023. Efficient wave type fingerprinting and filtering by six-component polarization analysis, *Geophys. J. Int.,* **234**(1), 25–39.

Suuster, E., Ritz, C., Roostalu, H., Reintam, E., Kõlli, R. & Astover, A., 2011. Soil bulk density pedotransfer functions of the humus horizon in arable soils, *Geoderma,* **163**(1–2), 74–82.

Takeuchi, H. & Saito, M., 1972. Seismic surface waves, *Methods Comput. Phys.,* **11,** 217–295.

Tanimoto, T., 1991. Waveform inversion for three-dimensional density and S wave structure, *J. geophys. Res.,* **96**(B5), 8167–8189.

Trampert, J., Deschamps, F., Resovsky, J. & Yuen, D., 2004. Probabilistic tomography maps chemical heterogeneities throughout the lower mantle, *Science,* **306**(5697), 853–856.

Trichandi, R., Bauer, K., Ryberg, T., Scherler, D., Bataille, K. & Krawczyk, C.M., 2022. Combined seismic and borehole investigation of the deep granite weathering structure—Santa Gracia reserve case in Chile, *Earth Surf. Process. Landform.,* **47**(14), 3302–3316.

Tuckwell, G., Grossey, T., Owen, S. & Stearns, P., 2008. The use of microgravity to detect small distributed voids and low-density ground, *Quart. J. Eng. Geol. Hydrogeol.,* **41**(3), 371–380.

Vantassel, J.P., Kumar, K. & Cox, B.R., 2022. Using convolutional neural networks to develop starting models for near-surface 2-D full waveform inversion, *Geophys. J. Int.,* **231**(1), 72–90.

Virieux, J. & Operto, S., 2009. An overview of full-waveform inversion in exploration geophysics, *Geophysics,* **74**(6), WCC1–WCC26.

Vossen, R.v., Trampert, J. & Curtis, A., 2004. Propagator and wave-equation inversion for near-receiver material properties, *Geophys. J. Int.,* **157**(2), 796–812.

Wielandt, E., 1993. Propagation and structural interpretation of non-plane waves, *Geophys. J. Int.,* **113**(1), 45–53.

Wu, G.-x., Pan, L., Wang, J.-n. & Chen, X., 2020. Shear velocity inversion using multimodal dispersion curves from ambient seismic noise data of Usarray transportable array, *J. geophys. Res.,* **125**(1), e2019JB018213.

Yuan, Y.O., Simons, F.J. & Bozdağ, E., 2015. Multiscale adjoint waveform tomography for surface and body waves, *Geophysics,* **80**(5), R281–R302.

APPENDIX

A. Finite difference error

Throughout this analysis we use 2nd order accurate formulations of the finite difference approximation of the 2nd spatial derivative of the wavefield quantity θ:

$$\frac{\partial^2 \theta}{\partial x^2} = \frac{\theta(x - \Delta x) - 2\theta(x) + \theta(x + \Delta x)}{\Delta x^2} - \frac{\Delta x^2}{24} \frac{\partial^4 \theta}{\partial x^4}. \tag{A1}$$

Following (Langston 2007a) we can calculate the error of this approximation due to the sampling for a sinusoidal wave by assuming a plane wave in the form

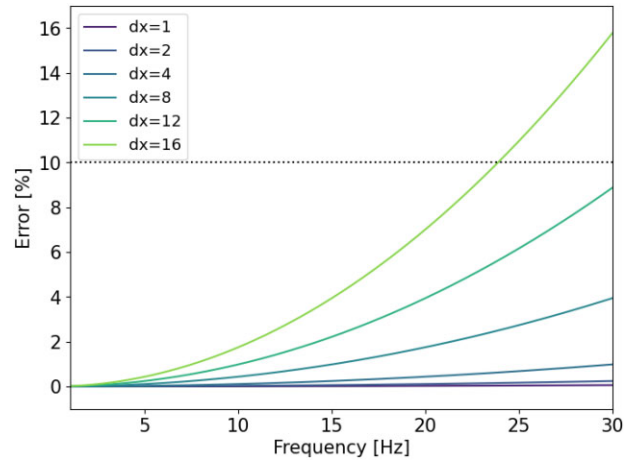$$\theta(x, t) = e^{i\omega(t - \frac{x}{c})}. \tag{A2}$$

We can then calculate the error ϵ (Fig. A1) based on the following formulation:

$$\epsilon = \left| \frac{-\frac{\Delta x^2}{24} \frac{\partial^4 \theta}{\partial x^4}}{\frac{\partial^2 \theta}{\partial x^2}} \right| = \frac{\Delta x^2 (2\pi)^2}{24 \lambda^2}. \tag{A3}$$

Setting an accuracy threshold ζ for the second derivative, the condition

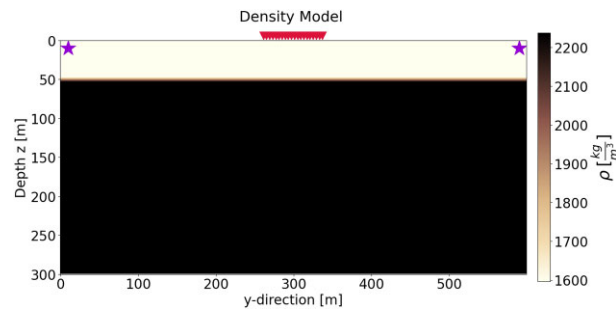$$\epsilon \leq \zeta \Leftrightarrow \Delta x \leq \sqrt{\frac{\zeta \, 24 \lambda^2}{(2\pi)^2}} \tag{A4}$$

implies the spacing Δx needs to be at most $0.247 \, \lambda$ to ensure an error lower than $\zeta = 0.1$.

Figure A1. Error evolution of the used finite difference approximation with frequency for different receiver spacings given in m. Black dotted line shows threshold error of 10 per cent. The wavelength is calculated for a velocity of 1550 m s^{-1}.

B. Reference density model

Figure B1. Reference density model depth cross-section in *yz*-plane. A constant density of 1600 kg m^{-3} is used for the top layer instead of the variable density structure imposed in Figs 3(c) and (d). 1600 kg m^{-3} corresponds to the mean value of the top layer in the variable density model.

## C. Frequency dependence of absolute density estimate
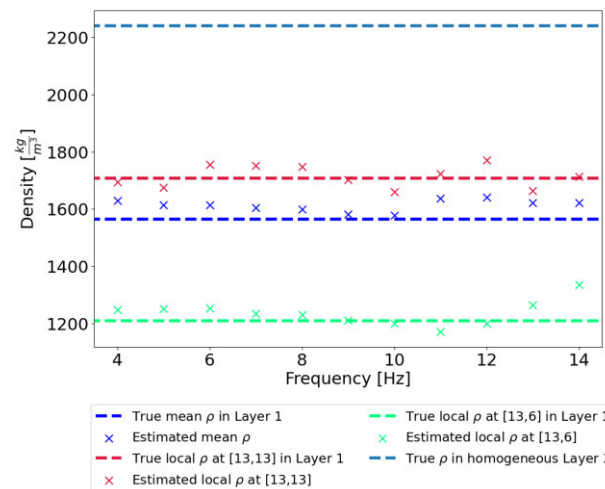
Figure C1. Frequency dependence of absolute density estimates obtained from full acoustic wave equation inversion. True model values shown at two local stations highlighted in Fig. 9, for example [13,13] (green dashed line) and [13,6] (red dashed line) and as a mean over all stations (dark blue dashed line). Estimates are shown as crosses in the respective corresponding colours. The light blue dashed line shows the density value of layer 2.

D. Acoustic parallel velocity and density gradient models
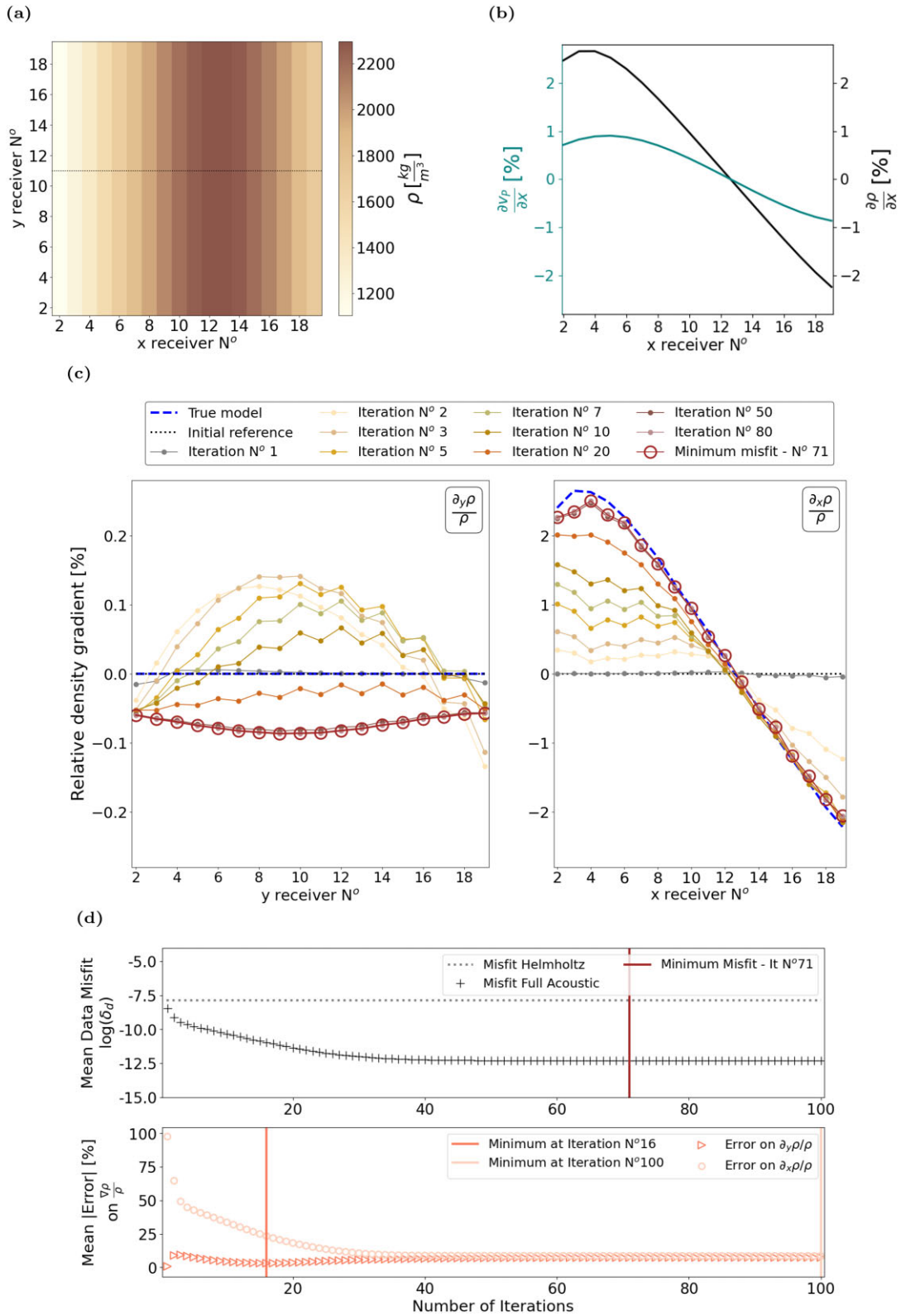
Figure D1. (a) True density model. Dotted black line indicates location of transect shown in panel (b). (b) True velocity (blue) and density (black) structure exhibit the parallel alignment of the gradients. Both velocity and density gradients follow the same sine curve but have different amplitudes. (c) Inverted relative density gradients $\nabla\rho/\rho$ in y- and x-direction, respectively. Results are obtained for a wavefield filtered between 7 and 9 Hz and are presented as mean value over all cross-sections in x-plane (left-hand panel) and y-plane (right-hand panel) and show the evolution at selected stages during 100 iterations. True model is depicted as dashed dark blue line and initial model as dotted black line. The minimum misfit result is highlighted by red circles. (d) Idem Fig. 6(c) with minimum misfit at iteration 71, and minimum parameter error on relative density y- and x-gradients at iteration 16 and 100, respectively.
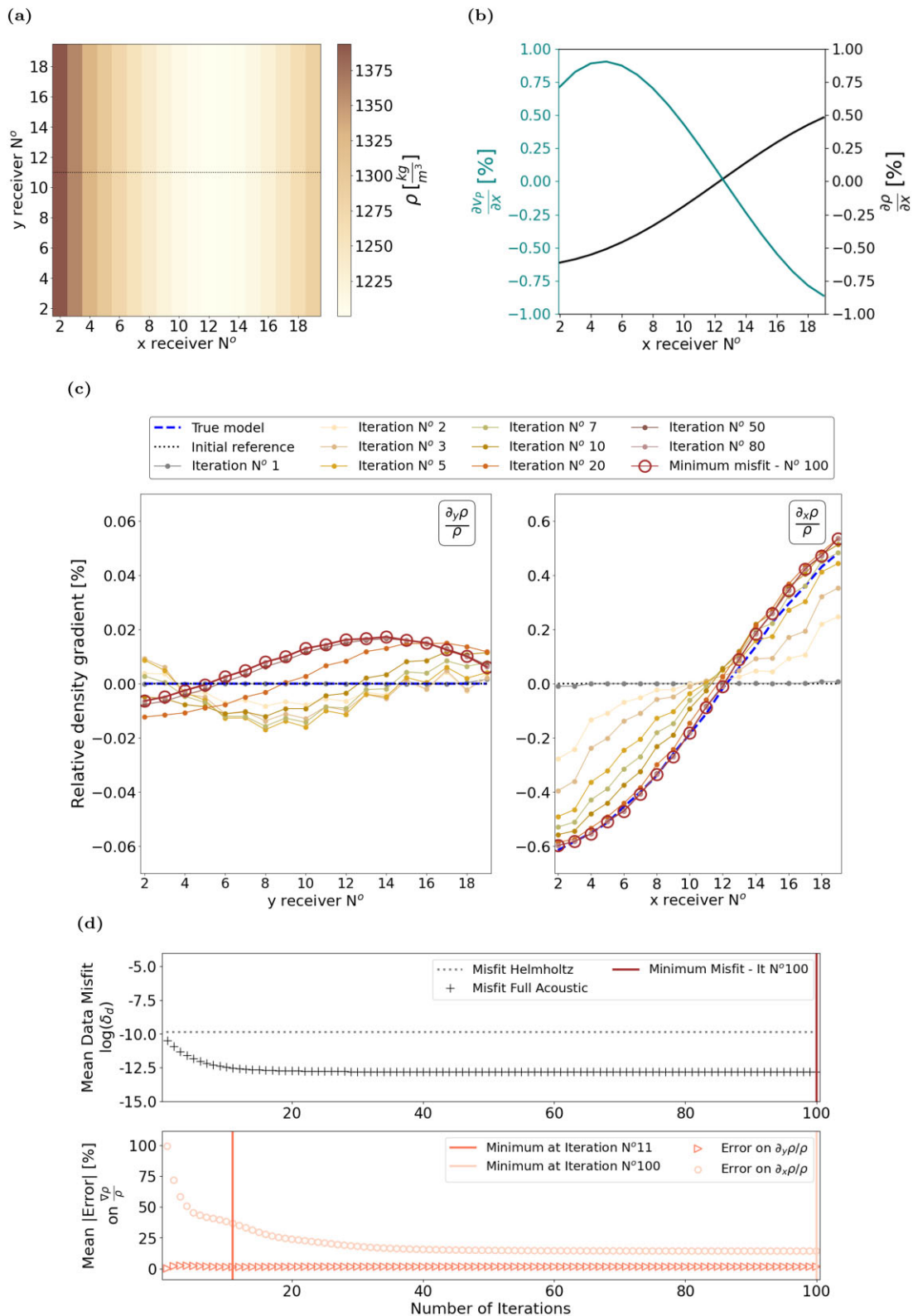
Figure D2. (a) True density model. Dotted black line indicates location of transect shown in panel (b). (b) True velocity (blue) and density (black) structure exhibit a variation in the same direction. Both velocity and density gradients are shifted with respect to each other but have similar amplitudes. (c) Idem Fig. D1(c). (d) Idem Fig. 6(c) with minimum misfit at iteration 100, and minimum parameter error on relative density *y*- and *x*-gradients at iteration 11 and 100, respectively.

E. Notes on the free surface methodology in inhomogeneous elastic media

In the body of this paper, all derivations from Newton's second law in eq. (1) are based on the assumption that Lamé parameters are constant over space (eq. 2a in elastic media and eq. 2b in acoustic media). For laterally varying Lamé parameters, these equations become:

$$\underbrace{\frac{(\lambda+2\mu)}{\rho}\left[\nabla(\nabla\cdot\boldsymbol{u})\right]-\frac{\mu}{\rho}\left[\nabla\times(\nabla\times\boldsymbol{u})\right]}_{\text{homogeneous terms}}+\underbrace{\frac{\nabla\lambda}{\rho}(\nabla\cdot\boldsymbol{u})+\frac{\nabla\mu}{\rho}\cdot\left[\nabla\boldsymbol{u}+(\nabla\boldsymbol{u})^T\right]}_{\text{inhomogeneous terms}}+\frac{\boldsymbol{f}}{\rho}=\partial_t^2\mathbf{u} \tag{E1a}$$

$$\underbrace{\frac{\lambda}{\rho}\left[\nabla(\nabla\cdot\boldsymbol{u})\right]}_{\text{homogeneous terms}}+\underbrace{\frac{\nabla\lambda}{\rho}(\nabla\cdot\boldsymbol{u})}_{\text{inhomogeneous terms}}+\frac{\boldsymbol{f}}{\rho}=\partial_t^2\mathbf{u}. \tag{E1b}$$

Here we investigate the effect that inhomogeneity has on the derivation of the equations in the free surface methodology used to estimate density and body wave velocities at the free surface presented in Section 2. Writing eq. (E1a) with all terms:

$$\underbrace{\frac{(\lambda+2\mu)}{\rho}\begin{pmatrix}\frac{\partial^2 u_x}{\partial x^2}+\frac{\partial^2 u_y}{\partial x\partial y}+\frac{\partial^2 u_z}{\partial x\partial z}\\ \frac{\partial^2 u_x}{\partial y\partial x}+\frac{\partial^2 u_y}{\partial^2 y}+\frac{\partial^2 u_z}{\partial y\partial z}\\ \frac{\partial^2 u_x}{\partial z\partial x}+\frac{\partial^2 u_y}{\partial z\partial y}+\frac{\partial^2 u_z}{\partial^2 z}\end{pmatrix}-\frac{\mu}{\rho}\begin{pmatrix}\frac{\partial^2 u_y}{\partial y\partial x}-\frac{\partial^2 u_x}{\partial^2 y}-\frac{\partial^2 u_x}{\partial^2 z}+\frac{\partial^2 u_z}{\partial x\partial z}\\ \frac{\partial^2 u_z}{\partial z\partial y}-\frac{\partial^2 u_y}{\partial^2 z}-\frac{\partial^2 u_y}{\partial^2 x}+\frac{\partial^2 u_x}{\partial x\partial y}\\ \frac{\partial^2 u_x}{\partial x\partial z}-\frac{\partial^2 u_z}{\partial^2 x}-\frac{\partial^2 u_z}{\partial^2 y}+\frac{\partial^2 u_y}{\partial y\partial z}\end{pmatrix}}_{\text{homogeneous terms}}$$

$$\underbrace{+\frac{1}{\rho}\begin{pmatrix}\frac{\partial\lambda}{\partial x}\\ \frac{\partial\lambda}{\partial y}\\ \frac{\partial\lambda}{\partial z}\end{pmatrix}\left(\frac{\partial u_x}{\partial x}+\frac{\partial u_y}{\partial y}+\frac{\partial u_z}{\partial z}\right)+\frac{1}{\rho}\begin{pmatrix}\frac{\partial\mu}{\partial x}\\ \frac{\partial\mu}{\partial y}\\ \frac{\partial\mu}{\partial z}\end{pmatrix}\cdot\left[\begin{pmatrix}\frac{\partial u_x}{\partial x}&\frac{\partial u_x}{\partial y}&\frac{\partial u_x}{\partial z}\\ \frac{\partial u_y}{\partial x}&\frac{\partial u_y}{\partial y}&\frac{\partial u_y}{\partial z}\\ \frac{\partial u_z}{\partial x}&\frac{\partial u_z}{\partial y}&\frac{\partial u_z}{\partial z}\end{pmatrix}+\begin{pmatrix}\frac{\partial u_x}{\partial x}&\frac{\partial u_y}{\partial x}&\frac{\partial u_z}{\partial x}\\ \frac{\partial u_x}{\partial y}&\frac{\partial u_y}{\partial y}&\frac{\partial u_z}{\partial y}\\ \frac{\partial u_x}{\partial z}&\frac{\partial u_y}{\partial z}&\frac{\partial u_z}{\partial z}\end{pmatrix}\right]}_{\text{inhomogeneous terms}} \tag{E2}$$

$$=\begin{pmatrix}\frac{\partial^2 u_x}{\partial t^2}\\ \frac{\partial^2 u_y}{\partial t^2}\\ \frac{\partial^2 u_z}{\partial t^2}\end{pmatrix}-\frac{1}{\rho}\begin{pmatrix}f_x\\ f_y\\ f_z\end{pmatrix}$$

we can use the free surface conditions

$$\frac{\partial u_z}{\partial z}=-\frac{v_p^2-2v_s^2}{v_p^2}\left(\frac{\partial u_x}{\partial x}+\frac{\partial u_y}{\partial y}\right) \tag{E3}$$

$$\frac{\partial u_y}{\partial z}=-\frac{\partial u_z}{\partial y} \tag{E4}$$

$$\frac{\partial u_x}{\partial z}=-\frac{\partial u_z}{\partial x} \tag{E5}$$

to derive the corresponding expression at the free surface. The expression of the homogeneous terms are described in (Curtis & Robertsson 2002) and the inhomogeneous terms become:

(i) Term 3 of eq. (E2)

$$\frac{1}{\rho}\begin{pmatrix}\frac{\partial\lambda}{\partial x}\\ \frac{\partial\lambda}{\partial y}\\ \frac{\partial\lambda}{\partial z}\end{pmatrix}\left(\frac{\partial u_x}{\partial x}+\frac{\partial u_y}{\partial y}-\frac{v_p^2-2v_s^2}{v_p^2}(\nabla_H\cdot\boldsymbol{u}_H)\right) \tag{E6}$$

(ii) Term 4 of eq. (E2)

$$\frac{1}{\rho}\begin{pmatrix}\frac{\partial\mu}{\partial x}\\ \frac{\partial\mu}{\partial y}\\ \frac{\partial\mu}{\partial z}\end{pmatrix}\cdot\begin{pmatrix}\frac{2\partial u_x}{\partial x}&\frac{\partial u_x}{\partial y}+\frac{\partial u_y}{\partial x}&\frac{\partial u_x}{\partial z}+\frac{\partial u_z}{\partial x}\\ \frac{\partial u_y}{\partial x}+\frac{\partial u_x}{\partial y}&2\frac{\partial u_y}{\partial y}&\frac{\partial u_y}{\partial z}+\frac{\partial u_z}{\partial y}\\ \frac{\partial u_z}{\partial x}+\frac{\partial u_x}{\partial z}&\frac{\partial u_z}{\partial y}+\frac{\partial u_y}{\partial z}&2\frac{\partial u_z}{\partial z}\end{pmatrix} \tag{E7}$$

$$=\frac{1}{\rho}\begin{pmatrix}\frac{\partial\mu}{\partial x}\\ \frac{\partial\mu}{\partial y}\\ \frac{\partial\mu}{\partial z}\end{pmatrix}\cdot\begin{pmatrix}\frac{2\partial u_x}{\partial x}&\frac{\partial u_x}{\partial y}+\frac{\partial u_y}{\partial x}&-\frac{\partial u_z}{\partial x}+\frac{\partial u_z}{\partial x}\\ \frac{\partial u_y}{\partial x}+\frac{\partial u_x}{\partial y}&2\frac{\partial u_y}{\partial y}&-\frac{\partial u_z}{\partial y}+\frac{\partial u_z}{\partial y}\\ \frac{\partial u_z}{\partial x}-\frac{\partial u_z}{\partial x}&\frac{\partial u_z}{\partial y}-\frac{\partial u_z}{\partial y}&-2\frac{v_p^2-2v_s^2}{v_p^2}\nabla_H\cdot\boldsymbol{u}_H\end{pmatrix} \tag{E8}$$

$$=\frac{1}{\rho}\begin{pmatrix}[\frac{\partial\mu}{\partial x}(\frac{2\partial u_x}{\partial x})]+[\frac{\partial\mu}{\partial y}(\frac{\partial u_x}{\partial y}+\frac{\partial u_y}{\partial x})]+0\\ [\frac{\partial\mu}{\partial x}(\frac{\partial u_y}{\partial x}+\frac{\partial u_x}{\partial y})]+[\frac{\partial\mu}{\partial y}(2\frac{\partial u_y}{\partial y})]+0\\ 0+0+[\frac{\partial\mu}{\partial z}(-2\frac{v_p^2-2v_s^2}{v_p^2}\nabla_H\cdot\boldsymbol{u}_H)]\end{pmatrix}. \tag{E9}$$

In our model, the receiver is buried at 1 m and the Lamé parameters do not change over the depth interval used for the calculation of the finite difference approximation of the first order depth derivative. We can thus consider the depth derivatives of Lamé parameters $\partial\mu/\partial z$ and $\partial\lambda/\partial z$ to be zero, and the inhomogeneous terms disappear in the vertical component of the full elastic wave equation at the free surface.